Summer 2020

Synthesis and Characterization of Carbon Coated Barium Titanate Core-Shell Nanoparticles

Moudip Nandi
Missouri State University, Moudip91@live.missouristate.edu

SYNTHESIS AND CHARACTERIZATION OF CARBON COATED BARIUM TITANATE CORE-SHELL NANOPARTICLES

A Master's Thesis

Presented to

The Graduate College of

Missouri State University

In Partial Fulfillment

Of the Requirements for the Degree

Master of Science, Materials Science

By

Moudip Nandi

August 2020

SYNTHESIS AND CHARACTERIZATION OF CARBON COATED BARIUM TITANATE CORE-SHELL NANOPARTICLES

Physics, Astronomy and Materials Science

Missouri State University, August 2020

Master of Science

Moudip Nandi

ABSTRACT

Core-shell nanoparticles (CSNP) with fascinating ferroelectric properties have diverse applications in biotechnology and the electronic field of studies. Among so many perovskites, barium titanate (BTO) nanoparticles draw much interest due to their distinct electronic and ferroelectric features. Additionally, the incorporation of carbon in the shell of CSNP makes it suitable for application in many fields due to its innocuous nature. Carbon not only increases the biocompatible properties of an element but also gives mechanical stability to the CSNP. This thesis is targeted towards the synthesis of oxide-carbide CSNP, where the core is made of BTO and the shell is made of carbon. The effect of nitrogen doping on these CSNP has also been investigated. Two unique techniques sono-chemical and pulsed laser ablation are used to synthesize the CSNP. X-ray diffraction (XRD) analysis indicates that the crystal structure of the core BTO nanoparticles remains intact.. Raman spectroscopy data shows the presence of all vibrational modes of BTO and carbon indicating the formation of CSNP. Scanning electron microscope (SEM) and energy-dispersive X-ray spectroscopic (EDS) analysis provide the surface morphology and the occupancy of prominent elements in the synthesized CSNP. The growth of carbon around the surface of BTO nanoparticles is confirmed through transmission electron microscopy (TEM). s. The line scan on high-resolution TEM (HR-TEM) images confirms the formation of CSNPs. To enhance the optical properties of synthesized CSNP, the shell was doped with a nonmetal like nitrogen. The contrast in the fluorescence spectra between the doped and un-doped samples confirms the incorporation of different functional groups and reveals the effect of nitrogen doping. The incorporation of various functional groups in the carbon shell of CSNP will help in targeted drug delivery applications.

KEYWORDS: core shell nanoparticles, barium titanate, carbon, Raman spectroscopy, X-ray diffraction, scanning electron microscopy (SEM), fluorescence spectroscopy

SYNTHESIS AND CHARACTERIZATION OF CARBON COATED BARIUM TITANATE CORE-SHELL NANOPARTICLES

By

Moudip Nandi

A Master's Thesis
Submitted to the Graduate College
Of Missouri State University
In Partial Fulfillment of the Requirements
For the Degree of Master of Science, Materials Science

August 2020

Approved:

Kartik Ghosh, Ph.D., Thesis Committee Chair

Ridwan Sakidja, Ph.D., Committee Member

Tiglet Besara, Ph.D., Committee Member

Julie Masterson, Ph.D., Dean of the Graduate College

ACKNOWLEDGEMENTS

I would like to thank my academic and research advisor Dr. Kartik Ghosh for immense support and guidance through two years of my research. He is always encouraging and supportive to take inventive approach while conducting the research. I am also grateful to Dr. Ridwan Sakidja for his help in SEM characterization. I thank my other committee member Dr. Tiglet Besara for his valuable suggestions.

I appreciate the help of my other friends specially Tauhidul Mohammad Islam, Bishwajit Karmakar, and Joy Roy for their help.

I dedicate this thesis to my parents Dr. Dilip Kumar Nandi and Mousumi Nandi

TABLE OF CONTENTS

LIST OF TABLES

LIST OF FIGURES

CHAPTER 1: INTRODUCTION

Nanotechnology fascinates many researchers with its attractive physical, chemical, and structural properties, and it can be applied in many fields of science such as physics, chemistry, material science, and medicine. Micrometer size materials do not exhibit drastic variation in their physical properties when it is in bulk size. However, the materials which are in a very small dimension (nanoscale) exhibits drastic changes in their physical properties. So a material does have minimal changes in its physical properties when it is in a bulk form. While the same material with nano-sizing exhibits varying physical and chemical properties. Thermal behavior, stability, solubility, and conductivity are among those physical and chemical properties of nanomaterials. Nanomaterials have a wide range of applications in electronic as well as biomedical industries. The unique physical and chemical properties of nanomaterials make them attractive elements in many biomedical applications such as drug delivery, biosensors, cell detection, etc. Based on dimension, the nanomaterials can be divided into three categories: nanoparticles (zero dimension materials), nanorods and nanowires (one-dimensional materials), and thin films, and nanosheets (two-dimensional materials).

Particles having a size in the nanometer range are referred to as ‘nanoparticles’. Where one nanometer is 10^{-9} m. Nanocrystal is one of the forms of nanoparticles, and when nanoparticles exist in crystal-like structures, they are referred to as ‘nanocrystals’. Nanoparticles have many unique properties due to quantum size effect, finite-size effect, and surface area effect. There is another form of nanoparticles which is termed as nanoclusters. The particle size of the nanoclusters is between 1 to 10 nm, and they can exhibit quantum size effects. Among so many types of nanoparticles, metallic nanoparticles are the most common and widely used.

Metallic nanoparticles have completely different electrical and chemical properties as compared to bulk metallic particles. The nanoparticles have a large surface to volume ratio, and due to this large surface to volume ratio, they exhibit tunable electrical and chemical properties. The light absorption band in most of the metallic nanoparticles is very large. The reason behind this large absorption band is due to the surface Plasmon absorption. The surface Plasmon absorption occurs when the particle size changes from tens to few nanometers. The oscillation of collective conduction electrons depends on the particle size and this change in an oscillation of collective conduction electrons referred to as surface plasmon absorption. Some kind of 'nanoparticles' are oxide-based, these oxides are mainly metal oxides and silicon oxides. Metal oxide nanoparticles are prepared from different elements like zinc oxide, titanium oxide, barium titanate, cobalt oxide, etc. Metal oxide nanoparticles have a wide range of applications in industries, they are used in cosmetic, pharmaceuticals, food processing, and food coloring industries. The high oxygen content in the earth atmosphere makes oxides the most stable materials. The main advantage of oxides is that they are mostly nontoxic, and this nontoxicity makes oxide materials more suitable for biological applications.

The properties of nanoparticles highly depend on the aggregation state, surface area, particle concentration, and surface charge. The aggregation state of nanoparticles depends on their aggregation tendency and the performance of the nanoparticles highly depends on their aggregation states. Nanoparticles have very low mass concentration though the percentage of the number of particle concentrations is very high. The delicacy of nanoparticles is directly proportional to the surface area. When the surface area increases the reactivity of nanoparticles also increases. The surface charge of the nanoparticles has a direct relationship with particle stability. As the properties of nanoparticles depend on these four factors, so any change in these

factors will lead to a change in the properties of nanoparticles. These factors are also size-dependent, that's why when a particle changes form micrometer to nanometer the properties of that particle also change. The individual and collective behavior of nanoparticles depend on the attractive or repulsive force between the nanoparticles. The particle size of a material is proportional to the volume of the particle, but it is inversely proportional to the number of atoms at the surface of the particle. So the decrease in particle size leads to decrement in particle volume, but there is an increment of the number of atoms at the surface of the particle. So the surface properties of nanoparticles are more adequate than the surface properties of bulk materials.

There are various synthesis procedures of nanoparticles. The synthesis of well dispersed nanoparticles is a very important. Different synthesis processes apply to different kinds of nanoparticles. Synthesis processes are mainly divided into three groups. Table-1 gives mainly three kinds of synthesis procedures, and these synthesis procedures are again subdivided into many synthesis methods. To get better control over the size of the nanoparticles wet chemical process is used. Among the wet chemical synthesis process, the colloidal chemistry method and phase transfer method are used to synthesize metallic nanoparticles and semiconducting nanoparticles. The fabrication of quantum dots from semiconducting materials is processed by the hydrothermal synthesis procedure. The main advantage of the wet chemical synthesis process is that it gives control over the kinetic and thermodynamic parameters and these parameters help get control over sizes and shapes of nanoparticles.

Table 1: Different synthesis methods

Synthesis Process	Methods
Wet Chemical Process	Hydrothermal, Sol-gel, Sono-chemical, colloidal chemistry and phase transfer methods
Physical process	Grinding, Milling, and Alloying
Gas-phase process	Laser ablation, Pyrolysis, and Plasma Synthesis

Through the milling process, large size particles are used to break into different shapes and size small particles. This process is easy, but there is a high chance of contamination. In the gas phase synthesis process nanoparticles are synthesized by three main methods laser ablation, pyrolysis, and plasma synthesis. Among these three processes, the laser ablation technique is very popular, and it is a more contamination-free process than the other methods. The main disadvantage of this process is that the amount of synthesized nanoparticles is very low. Different synthesis techniques have their advantages and disadvantages but it is very important to choose a suitable synthesis method to avoid contamination.

The main problem of nanoparticles is that they tend to agglomerate with each other. Agglomerated nanoparticles act as micro particles and lose their functionality. To eliminate this problem researchers invented the concept of CSNP. CSNP are biphasic, and they improve the functionality of nanoparticles. In CNSP the core and the shell part have consisted of different materials. The nanoscale coating of shell over the core material gives stability to the core. Due to the presence of the shell portion, the chance of agglomeration for CSNP is less than the normal nanoparticles. CSNP also increases the functionality of the nanoparticles. There are many possible combinations of CSNP that can be prepared. Some of them are inorganic core and organic shell

material, inorganic core and inorganic shell material, metallic core and metallic shell material, metal oxide core and biocompatible shell material. Figure 1 represents a conventional schematic diagram of the CSNP. Here the blue colored portion represents the core and the orange-colored portion represents the shell. The core and shell elements are different so they are represented with different colors.

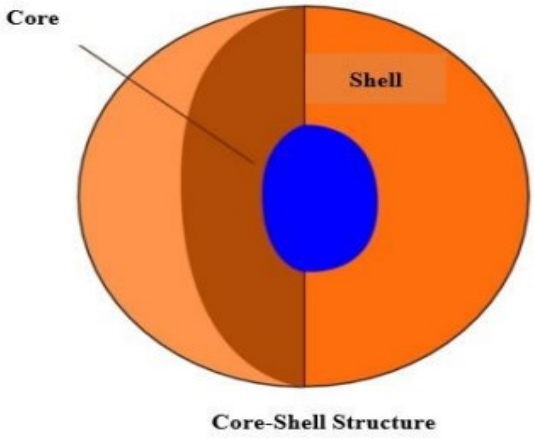

Figure 1: Conventional Schematic diagram of core shell nanoparticle

Below Figure 2 represents different types of CSNP. The 1st one represents a single-core and single shell-like structure. The 2nd diagram represents the hexagonal core and hexagonal shell structure. The 3rd diagram represents multiple cores and a single shell coating structure. The 4th diagram represents Nanomatryushka material where the core is located in the middle of two shells. The last diagram represents a moveable core inside a hollow shell structure

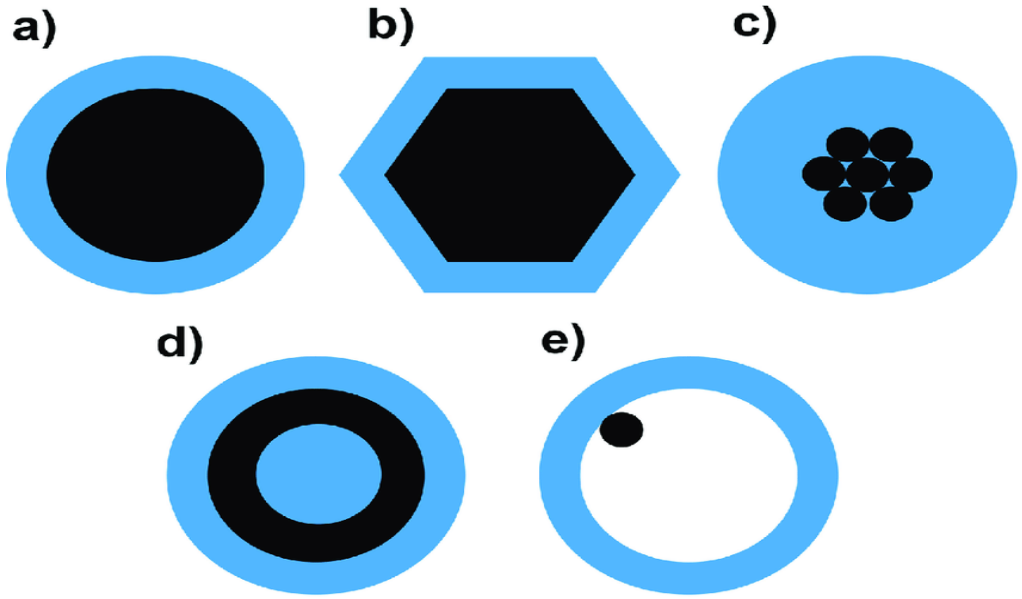

Figure 2: Different structure of core- shell nanoparticles

In this thesis, the phase 1 of the project is based on CSNP, and here BTO was used as the core material, it is necessary to discuss the crystal structure and the usefulness of BTO. BTO has a perovskite crystal structure. The chemical formula of the perovskite crystal structure is ABO_3. A represents the cations which are mainly located at the corner of the crystal structure. B represents the smaller cations that are situated in the middle of the structure. Anions are mainly oxygen and they are situated at the center of the face edges. Below Figure 3 is the schematic diagram of perovskite BTO. Here the green atoms represent the cations which are mainly located at the corner of the perovskite crystal structure. The grey colored atom is the smaller cations titanium, and it is located in the middle of the perovskite structure. Oxygen atoms which are anions are located at the center of each face edge. BTO is an inorganic chemical compound. The color of BTO is white and it has both ferroelectric and piezoelectric properties. M.H. Frey and D.A. Payne reported the grain size dependency on structure and phase transformation for

BTO[1]. They have mentioned the structures and properties of thin layer BTO which deviates from its bulk and single crystal forms.

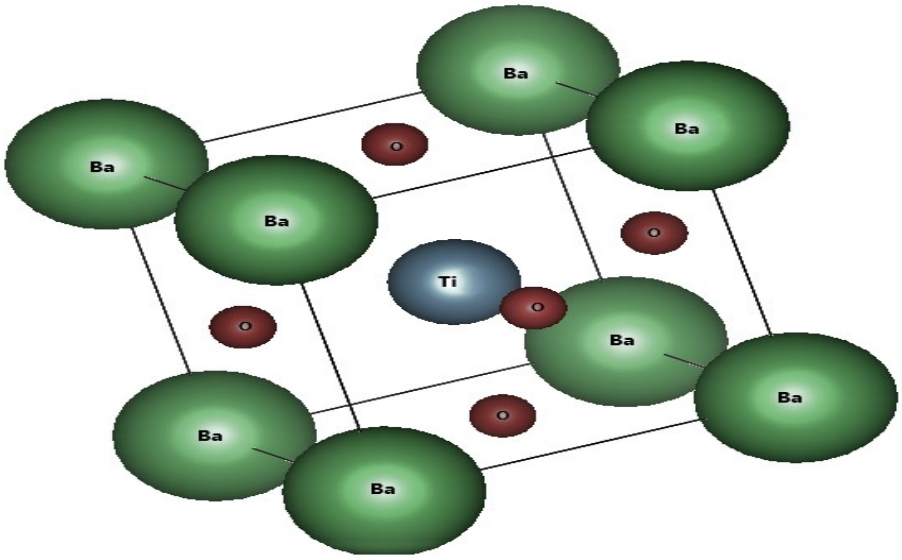

Figure 3: Schematics of Perovskite structure of BTO

Another interesting fact about BTO is that it has different kinds of crystal structures above and below Curie temperature. The temperature-dependent crystal structures of BTO exhibit different unique properties. That's why it is one of the popular materials in many applications. There are so many applications on BTO in ceramic capacitors especially multilayer ceramic capacitors due to its high dielectric constant and low loss characteristics[2]. Also, it has many wide applications such as infrared detectors, piezoelectric transducers, electro-optic devices, etc. These unique attractive properties and many scientific applications are the main motivation to use BTO as a core element in this research work.

Phase 1 of this research work is based on the synthesis of carbon coating on the BTO surface. The synthesis procedure is novel and normal sugar is used as the carbon source. Guiqin

Wang* and Xiaodong Chen presented a work based on BTO and carbon-based composite materials[3]. In their work it represented that carbon interaction with BTO increases electromagnetic properties of the composite material. There are several research works based on carbon as carbon is one of the popular material and exhibits good optical properties. Kehinde Olurode and Gururaj M. Neelgund published a paper based on carbon coating on titanium oxide nanoparticles[4]. So there are possibilities that carbon may show good binding quality with BTO. The shell of carbon over the surface of BTO not only enhances optical properties but also makes it biocompatible. Carbon-coated biocompatible BTO nanoparticles can be used as cell detection and biosensing applications. The carbon on the surface of BTO can act as a connector between organic and inorganic materials, which means any kind of doping is possible on the carbon layer. The carbon coating over the BTO surface also increases the mechanical stability of BTO nanoparticles. These advantages of carbon are the main motivation to be the shell material in this research work. The proposed diagram of the synthesized carbon coated BTO nanoparticles are depicted in Figure 4.

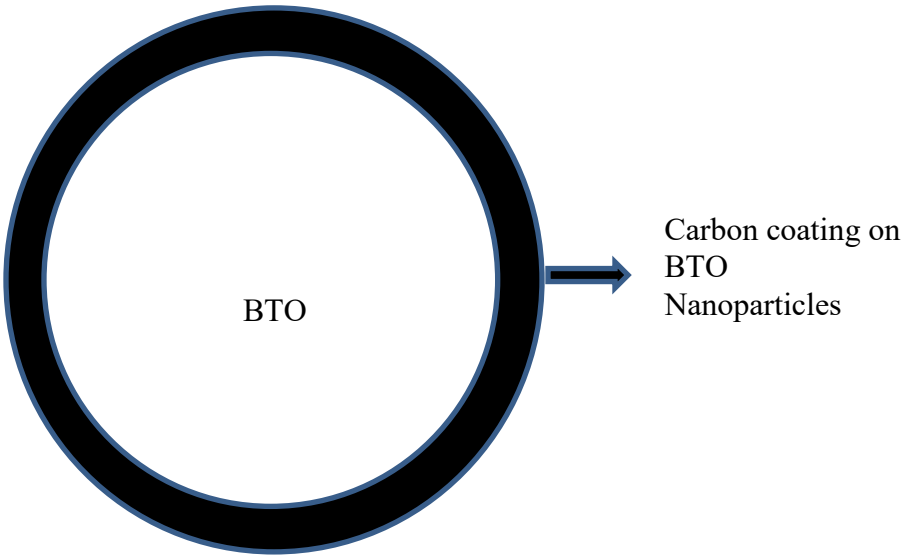

Figure 4: Proposed diagram of core shell nanoparticles

The second phase of this research work is based on nitrogen doping over the CSNP. A nonmetallic element like nitrogen have good bonding properties with carbon, which enhances the optical properties of carbon[5]. There are several studies based on the effect of nitrogen doping over graphene. These studies give information about the qualitative enhancement of Raman spectroscopy of graphene[6]. Zhen-Long Zhang and Jun Feng Li published a paper on perovskite solar cells made of titanium oxide. In their report, they used nitrogen doping on titanium oxide to extend the visible light absorption rate[7]. It can be concluded that nitrogen doping is an efficient process to reduce bandgap and enhance optical properties. In this research work, two synthesis procedures are mainly used for the creation of CSNP and nitrogen doping. To confirm the formation of CSNP, some characterization techniques like XRD, Raman spectroscopy, TEM, and UV-VIS are used in the phase one of this research work. The XRD, Raman, SEM and Fluoresce characterization techniques are used to confirm the nitrogen doping on CSNP in the 2^{nd} phase of this research work.

CHAPTER 2: SYNTHESIS AND CHARACTERIZATION OF CORE-SHELL NANOPARTICLES BY SONO-CHEMICAL METHOD

2.1 Abstract

A unique sono-chemical approach was adopted to develop the carbon coating on a popular perovskite material like BTO. Glucose was used as the carbon source due to its numerous arability in the market. The XRD characterization technique is used to evaluate the crystal structure of the synthesized CSNPs. The XRD analysis and TOPAS fitting reveal the formation of tetragonal BTO. This tetragonal structure of BTO remains unaltered after carbon coating. The information about the vibrational modes present in BTO and carbon coated BTO is extracted from Raman spectroscopic analysis. The results from the Raman spectra provides the information about the presence of carbon in the synthesized core-shell nanoparticle and its bonding with BTO. The normal sugar was annealed to see the Raman spectra of carbon extracted from sugar. The Raman spectra of synthesized CSNP and Raman spectra of carbon, which is extracted after annealing the sugar, are compared with each other to see the optical properties of carbon. UV-VIS spectroscopy analysis helps evaluate the transmission and absorption spectra of these nanoparticles. The surface topological analysis is performed by SEM, and the line scan of EDS confirms the presence of prominent materials in the synthesized CSNP.

2.2 Introduction

In recent years most important research areas are based on the core-shell nanomaterials and nanostructures. The core-shell nanomaterials and nanostructures have good potential applications in various fields like industrial, catalysts, and biomedical applications. These kinds

of nanomaterials and nanostructures may consist of different sizes of nanocomposites. The size of the CSNP depends on the shape of the core and shell thickness with different surface morphology. Based on shapes these particles can be spherical, centric, eccentric, star-like, or tubular. The properties of these particles can be tuned by making a change in their shape and size, this property tuning helps convert these nanocomposites from one material to another. Those nanoparticles which have their surface modified by functional groups or molecules or coated with a thin layer of other material show unique properties than non-functionalized uncoated nanoparticles. There can be various combinations of core-shell structures possible like 1) metal core and different metal shell 2) metal core and nonmetal shell 3) nonmetal core and nonmetal shell 4) organic core and inorganic shell etc.

There are some studies based on the synthesis and characterizations of oxide-oxide, oxide-sulfide based core-shell nanoparticles. In this paper, we focus on the synthesis and characterization of oxide-carbide based CSNP, where the core is made of BTO and the shell is made of C. The choice of materials for the core as well as shell depends on the properties and applications. There has been increased interest in chemical synthesis of Nano-scaled ferroelectric oxides, and BTO is one of them. Ferroelectric materials have applications in transducers, actuators, capacitors, and memories. Ferroelectric material shows ferroelectricity, which is a characteristic of certain materials that have spontaneous electric polarization. This spontaneous electric polarization can be reversed by applying an external electric field[8]. Many of these ferroelectric materials are pyroelectric and they have pyroelectric characteristics. These kinds of materials can generate a temporary voltage when they are heated or cooled. Spontaneous polarization is a fundamental property of pyroelectric crystals, but only in ferroelectric materials this polarization can be reversible and reorient able. It can be easily inferred that all ferroelectric

materials are pyroelectric, but all pyroelectric materials are not ferroelectric. BTO has both ferroelectric and pyroelectric properties. It has different kinds of structures, and these structures have different kinds of electric properties. The cubic and hexagonal structures of BTO are para electric while the other structures like tetragonal, rhombohedral, and orthorhombic are ferroelectric. At a certain temperature called Curie temperature, cubic BTO structure transforms from para electric to ferroelectric tetragonal structure. This transformation creates internal stress in BTO which affects some properties of this material. BTO has high dielectric constant and low loss characteristics which makes it a popular choice in capacitor industries. So many capacitors and multilayer capacitors are made off BTO. In pure form, BTO acts as an insulator, but after doping with some other materials it shows semi conductive features[9]. This makes BTO an attractive element in semiconductor-based industries. Large polarization, large permittivity, and large induced strain like important properties make BTO a potential candidate for field-induced piezoelectric transducers and sensors[10]. Due to its attractive features and a vast range of applications, BTO is a popular choice as a core material in our CSNP.

In CSNP, the choice of shell materials depends on the end application. The shell made of different materials also gives stability to the CSNP. Among so many shell materials carbon is an attractive one due to its good optical properties and excellent binding affinity with oxides[11]. Carbon is a biocompatible element too. Carbon can be used as an interlink between organic and inorganic materials. So any kind of organic or inorganic materials can be doped on the surface of CSNP with carbon as a shell material. We used normal sugar as our carbon source. The sol-gel method, hydrothermal, and emulsion polymerization are some conventional approaches to synthesize CSNP. Herein, we used a unique and simple synthesis technique. To characterize this

BTO and carbon-based CSNP XRD and Raman spectroscopy are used. These two methods are very useful to determine the structural and optical properties of CSNP.

2.3 Methodology

2.3.1 Materials. Pure BTO and normal sugar ($C_{12}H_{22}O_{11}$) are the primary materials used to prepare these CSNP. Acetone (C_3H_6O), Ethanol (C_2H_5OH), and deionized water are among those secondary materials which are used in this core-shell nanoparticle preparation. Pure BTO with average particle size of 50nm and purity of 99.95% were brought from Inframat Advanced Materials, USA. Normal sugar was brought from the market. All chemicals were used without further purification.

2.3.2 Dispersion of Particles. Pure $BaTiO_3$ (77.8 mg) and sugar (1711.5 mg) were mixed with DI water (20 ml) and placed on bath sonicator for 3-4 hrs. The dispersion of these two different kinds of particles was undertaken by the sonication process. Bath sonicator helped in coting BTO nanoparticles with sugar.

2.3.3 Removal of Contamination. The sugar-coated BTO nanoparticles are fetched by centrifugation procedure. This process continued for 10-15 minutes at 800 rpm speed which help separate the particles from DI water. Centrifugation followed by acetone and ethanol wash, acetone, and ethanol (2-3ml) were added to the particles this addition produce a mixture of acetone ethanol and particles. Then the mixture was kept on a hot plate for 15-20 min. The heat helped the alcohol evaporate and the particles were left as remaining material.

2.3.4 Synthesis of Carbon Coated Nanoparticles. After removing contamination, the particles were collected on a crucible, the crucible was wrapped with aluminum foil, and then it was placed inside a tube furnace. Inside the tube furnace, the particles were heated up to 400^0C

and kept for 2hrs in the argon atmosphere. Due to this high-temperature heating H_2O evaporated from sugar and left as carbon. This carbon nucleates on the surface of BTO and creates the coating. The argon gas prevented carbon to get oxidized. In the final step, this carbon coated BTO CSNPs were taken from the tube furnace and were collected on tubes. Below Figure 5 is the flow chart of this synthesis process.

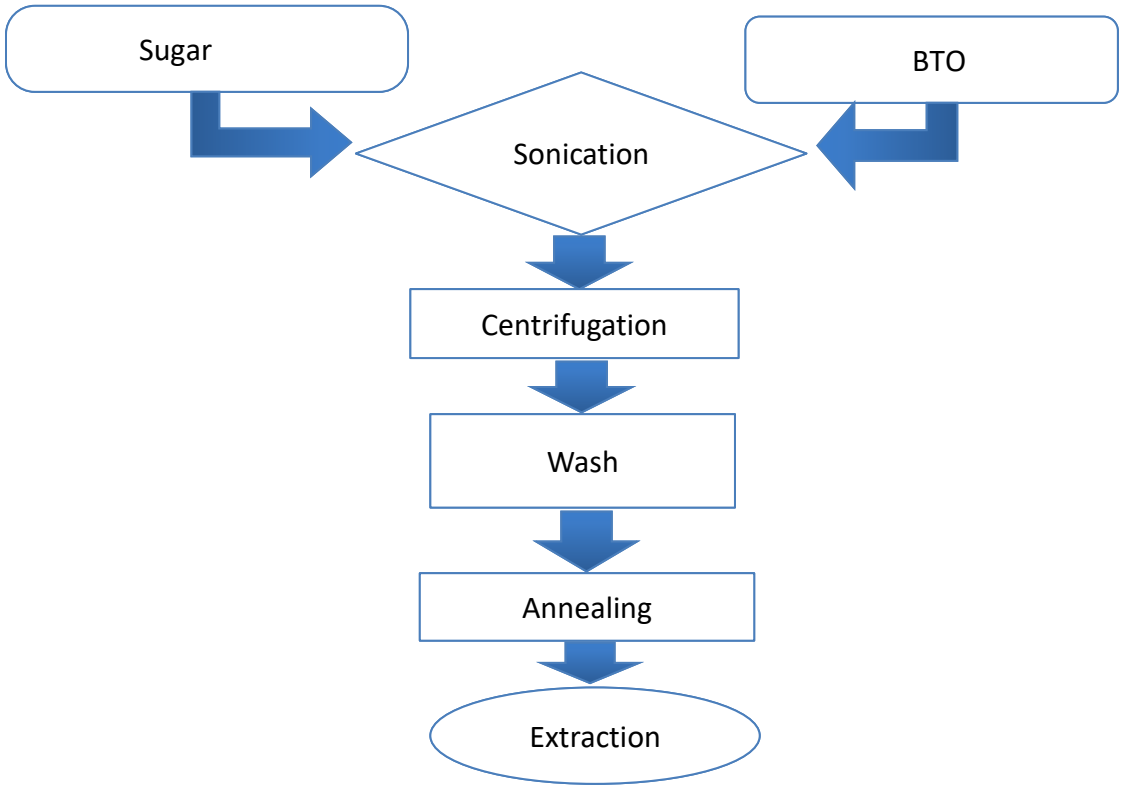

Figure 5: Flow chart of synthesis procedure

2.4 Characterization

The obtained sample was characterized by using XRD (Brucker, D8 Discover) to get some information about its diffraction patterns. The θ-2θ scan was done with CuK_α (λ=1.5405 angstrom). The Rietveld refinements were executed by Diffrac^{plus} TOPAS software. Raman

spectroscopy was carried out to gain information about the vibrational modes. The Raman spectroscopy was analyzed by NSG Lab spec software. Surface topological analysis was carried out by SEM, and confirmation of elements was done by EDX.

2.5 Results and Discussion

2.5.1 XRD. The XRD patterns of carbon-coated BTO nanostructures were characterized using X-ray powder diffraction (Bruker, D8 Discover; θ-2θ scan with Cu Kα (λ = 1.5405 Å)). The analysis of XRD data was performed using Rietveld refinement. TOPAS software was used to perform this Rietveld refinement. Below Figures 6 (a) and (b) are the fitted XRD plot of pure BTO and carbon-coated BTO, where the observed, calculated (by Rietveld refinement) and the difference are represented by black, red, and blue colors, respectively.

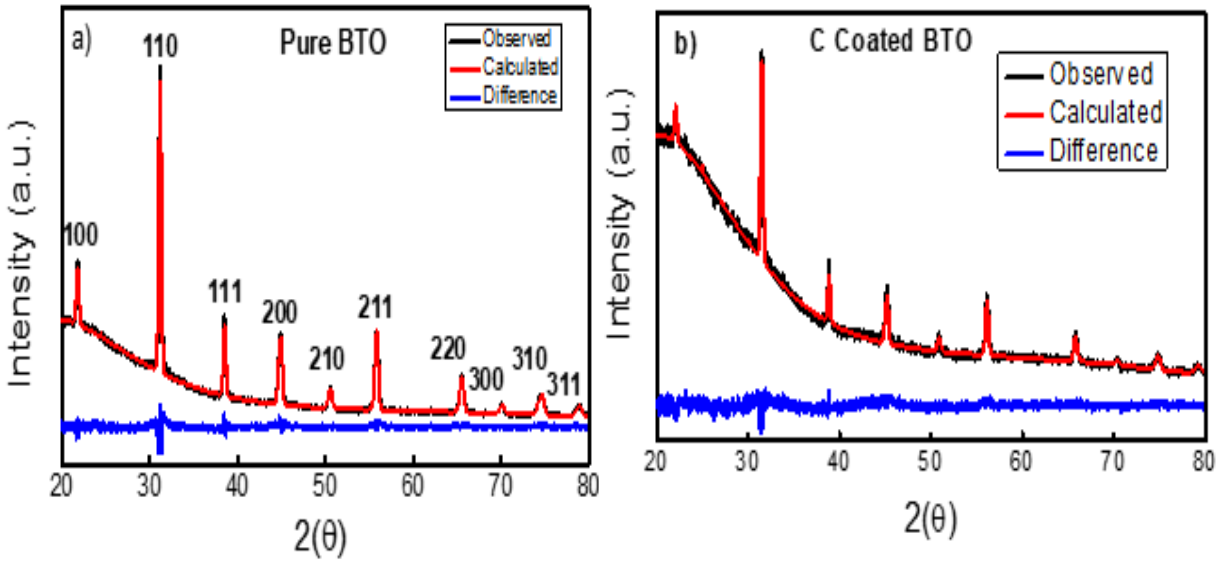

Figure 6: Fitted and experimental XRD plots of pure BTO (a) and BTO+C (b)

During this Rietveld refinement, extreme care was taken to minimize the influence of background. Besides this minimization of background influence, two major parameters are very important for this refinement process: one is the correct peak shape profile functions and the other is the structural and peak profile limitations. The indication of the accuracy of this refinement was judged by the goodness of fit (GOF) values and agreement indices (R values) values. To make this refinement parameters more accurate the emission profile was set for all possible CuKα radiations. In Chebychev's background correction an order of 8 was employed, this order was the order of the polynomial. The zero error and absorption correction factors were considered during this refinement process. The peak profile functions are the fundamental parameter in this refinement process. The number of variable parameters was carefully chosen to avoid anomalous results. In the XRD experiment, the powder sample was placed according to the Bragg-Brentano reflection geometry[12]. Before the collection of XRD data, certain conditions were considered, mainly the geometry of the XRD instrument, axis alignment of the sample, the sample thickness, and a suitable data acquisition time. The crystallite size was determined by using the Scherrer equation. The crystallite size of pure BTO is 18nm while the crystal size of carbon-coated BTO is 21nm.

From the XRD data it is clear that the diffraction peaks are present at $2\theta = 21.75^0$, 31.35^0, 38.42^0, 44.89^0, 50.64^0, 55.80^0, 65.52^0, 70.07^0, 74.62^0 and 78.94^0. The XRD pattern matches with the tetragonal crystal structure, having space group symmetry of *P4mm*[13]. X-ray powder diffraction is sensitive to crystalline materials but not to amorphous materials. As carbon has an amorphous state, so in Figure 6 (a) the XRD pattern is associated with BTO only. There is a gap between the starting intensities of pure BTO and carbon coated BTO which is intelligible in Figure 6 (b). This gap is due to the amorphous nature of carbon. The XRD pattern of carbon-

coated BTO displays low-intensity peaks corresponds to pure BTO. This is due to the presence of carbon coating on BTO which may act like a mask resulting a reduction in the intensity of diffraction peaks[14]. It is quite clear from Table 2 and Table 3 that there is hardly any difference in the lattice parameters of pure BTO and carbon coated BTO.

Table 2: Lattice Parameters of Pure BTO

2θ (^{0})	hkl	d_{hkl} (Å)	a (Å)	b (Å)	c(Å)	α(^{0})	β(^{0})	Υ (^{0})
21.75	100	4.039	3.99	3.99	4.02	90	90	90
31.35	110	2.835	3.99	3.99	4.02	90	90	90
38.42	111	2.313	3.99	3.99	4.02	90	90	90

Table 3: Lattice Parameters of BTO@C

2θ (^{0})	hkl	d_{hkl} (Å)	a (Å)	b (Å)	c(Å)	α(^{0})	β(^{0})	Υ (^{0})
21.75	100	4.039	4.00	4.00	4.01	90	90	90
31.35	110	2.836	4.00	4.00	4.01	90	90	90
38.42	111	2.31	4.00	4.00	4.01	90	90	90

These results reveal the fact that there is no epitaxial growth of carbon on the surface of BTO. The amorphous like carbon is only covered on the BTO surface as a shell element.

2.5.2 Raman Spectroscopy. The Raman spectra of pure BTO and carbon coated BTO are presented in below Figures (Figure 7 (a) and (b)). Backgrounds were subtracted to reduce the

noise and visualize the peaks prominently in the Raman data. We did deconvolution on the peaks using Origin software to see whether there is any presence of multiplicity. The Raman spectra for both pure BTO and carbon coated BTO were recorded in the range of 100-2000 cm^{-1} with the laser excitation wavelength of 532 nm. Based on the crystallography, Raman active modes for tetragonal BTO (*P4mm*) are 4E (TO+LO) +3A_1 (TO+LO) + 1B_1 (TO+LO), while no Raman phase is predicted for the cubic phase (*pm3m*). In the tetragonal phase, these Raman modes occur due to the splitting of F_{1u} and F_{2u} modes. The F_{1u} mode splits into one $A_1$and one E mode, and the F_{2u} mode splits into B_1 and E modes [12]. These modes further split into longitudinal and transverse optical modes. The appearance of these modes is due to the presence of large electrostatic forces that are associated with lattice iconicity. The polarization of the A_1 phonon is parallel with the *z*-axis, and E_1 phonons are polarized in the *XY* plane. The propagation of phonon in the *XY* plane consists of an A_1 transverse, E_1 transverse, and E_1 longitudinal wave. There is a frequency difference between A_1 transverse phonon and E_1 transverse phonon, and this frequency difference is due to the effect of anisotropic force. The mixture of transverse and longitudinal wave phonons move in arbitrary directions, but only the E_1 transverse phonon which is an ordinary transverse phonon polarizes normal to its propagation direction and *z*-axis. As the electrostatic forces are much greater than anisotropic force, the mixing of transverse and longitudinal waves is minimal in some extraordinary waves. Due to this fact, these waves can be separated very easily. The difference in peak intensity is caused by the nature of the electron-phonon coupling. Owing to the same contributions to the order of magnitude, it can be additive or subtractive. The changes in polarizability values and Raman peak intensities are significantly different for transverse and longitudinal waves. In Figure 7 (b) the peaks at 189.92, 250.30, 306.81, 520.34, and 711.92cm^{-1} are associated with Raman spectra of pure BTO. These peaks are

associated with different vibration modes. The peaks at around 250 cm^{-1} and 304 cm^{-1} are due to the vibration of the TiO_6 group, and the peak at around 514 cm^{-1} is due to the occurrence of vibration by displacement of oxygen atoms. The Raman peak at around 303 cm^{-1} is the characteristic of the tetragonal crystal structure of BTO. This peak is due to the overlap of E (3TO) + E (2LO) +B_1, and the intensity of this peak decreased with an increase in temperature.

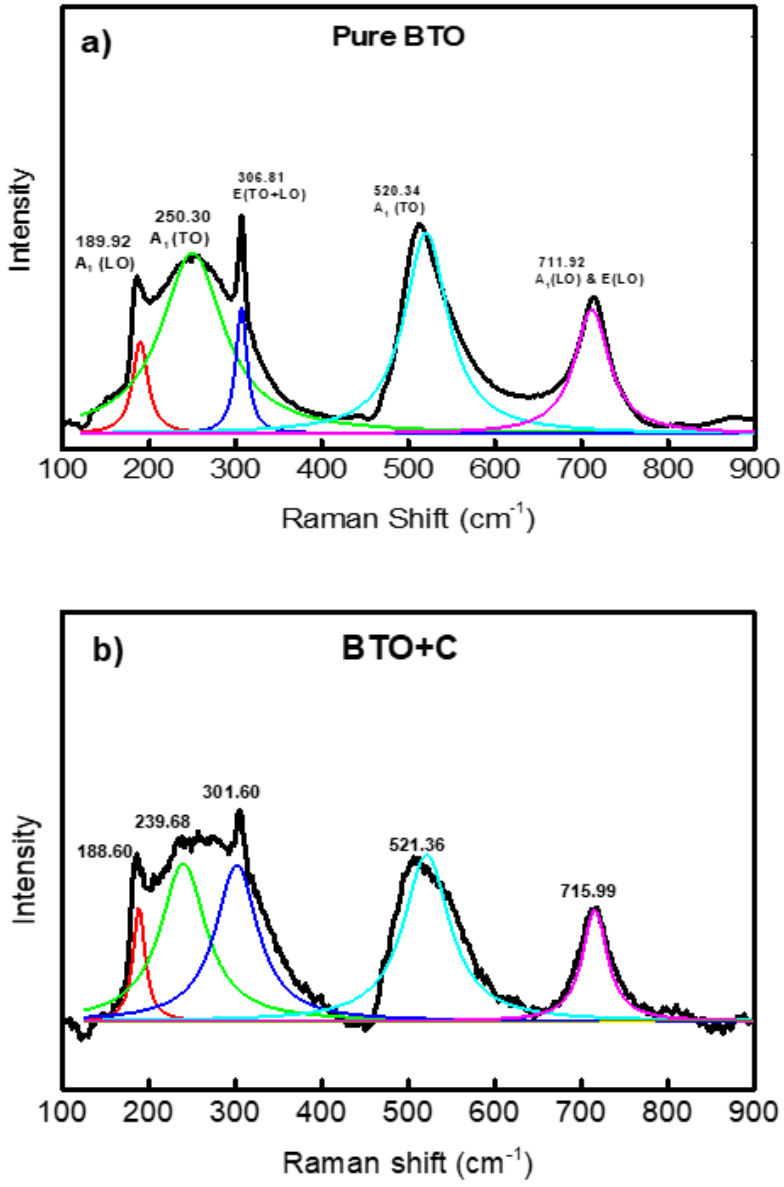

Figure 7: Fitted and background subtracted Raman spectra of pure BTO (a) and BTO+C (b)

As the carbon coating was performed under high temperature at 400^0C inside the tube furnace, it is quite clear from Figure 7(b) that the intensity of the Raman peak of carbon coated BTO at around 303 cm^{-1} is lower than the intensity of the Raman peak of pure BTO. The Raman peaks at carbon coated BTO are not at the same position when they are compared with pure BTO. In carbon coated BTO the peaks are shifted. This shift is due to the optical phonon confinement effect, and this effect is prevailingly larger in nanostructures. Crystal defects can also be a reason for this Raman shift. Oxide nanomaterials have many structural defects (oxygen vacancy) that affect their optical properties. This oxygen vacancy has a proportional relationship with lattice distortion that is with the increase in oxygen vacancy the lattice distortion also increases. This distortion of lattice causes the loss of transitional symmetry, and for this reason, the phonons are not restricted to originate from a point near the Brillouin zone center. So that the phonons can originate anywhere in the Brillouin zone provided their wave vectors add up to approximately zero. It can be concluded that these Raman shifts occur due to either defect in lattice or dispersion of large size nanoparticles. So the smaller diameter nanoparticles contribute more to the spectrum. The shift of phonon frequencies towards higher/lower values depends upon the presence of tensile/compressive stress. The width of the Raman peaks in carbon coated BTO is also broadening in comparison with pure BTO due to change in crystallinity and molecular structure. The Raman peak shift of carbon-coated BTO indicates the interaction of BTO nanostructures with carbon. Due to this interaction, there are changes in atomic structures as well atomic vibration. Below Figure 8 and Figure 9 are the Raman spectroscopy data of carbon from BTO+C and sugar. To do the comparison between two carbons, we annealed normal sugar inside the tube furnace at 400^0C resulting a complete conversion from sugar to carbon. We recorded Raman spectroscopy data in the range of 100-2000 cm^{-1}. In this particular range there were no

peaks of C which are present in pure BTO, but there were two peaks at around 1340cm^{-1} and 1590cm^{-1} which are present in BTO+C. In Figure 9 the Raman peaks are similar with the Raman peaks in BTO+C. These two clear peaks around 1340 and 1570 cm^{-1} are due to the stretching modes of D band and G band respectively. The breathing modes of K-point phonons of A_1g symmetry are the main reason of this D band and the G band, due to this the in-plane bond-stretching motion of the E2g phonon of Carbon sp^2 atoms. The intensity of the D band is related to the defects and disorder present in the crystal structure. The intensity ratio between the D band and G band (I_D/I_G) helps to evaluate the ordered and disordered structure of graphite. The (I_D/I_G) value of C coated BTO is 0.85, so it can be inferred that there is a possibility of an ordered graphitic carbon shell formed on BTO nanoparticles.

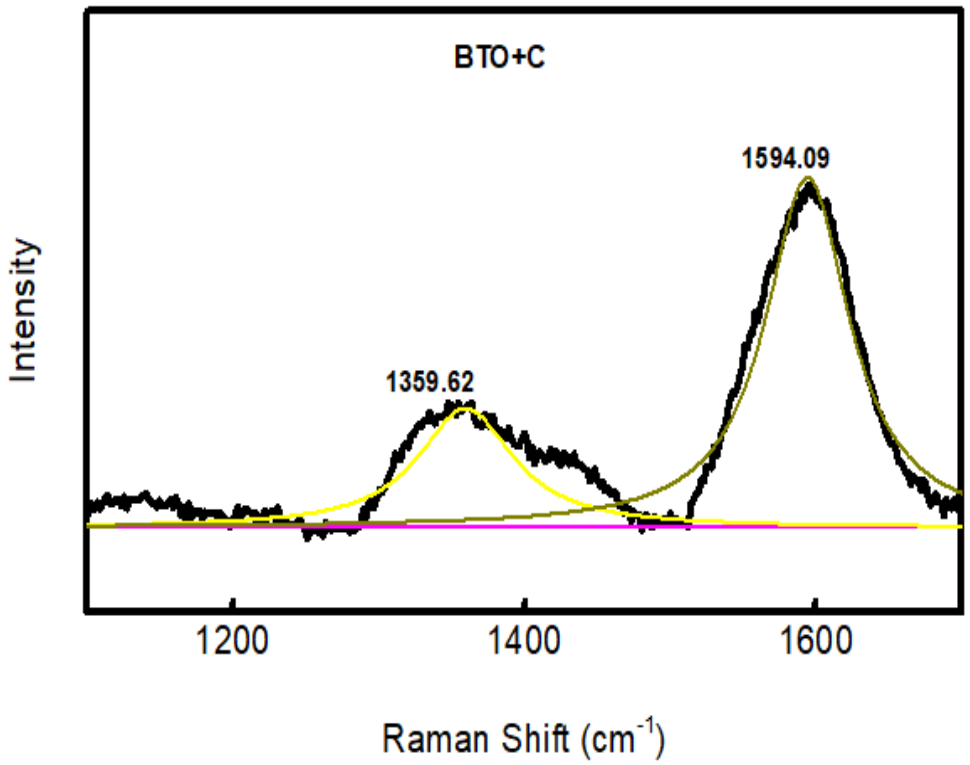

Figure 8: Raman spectra of C from BTO+C

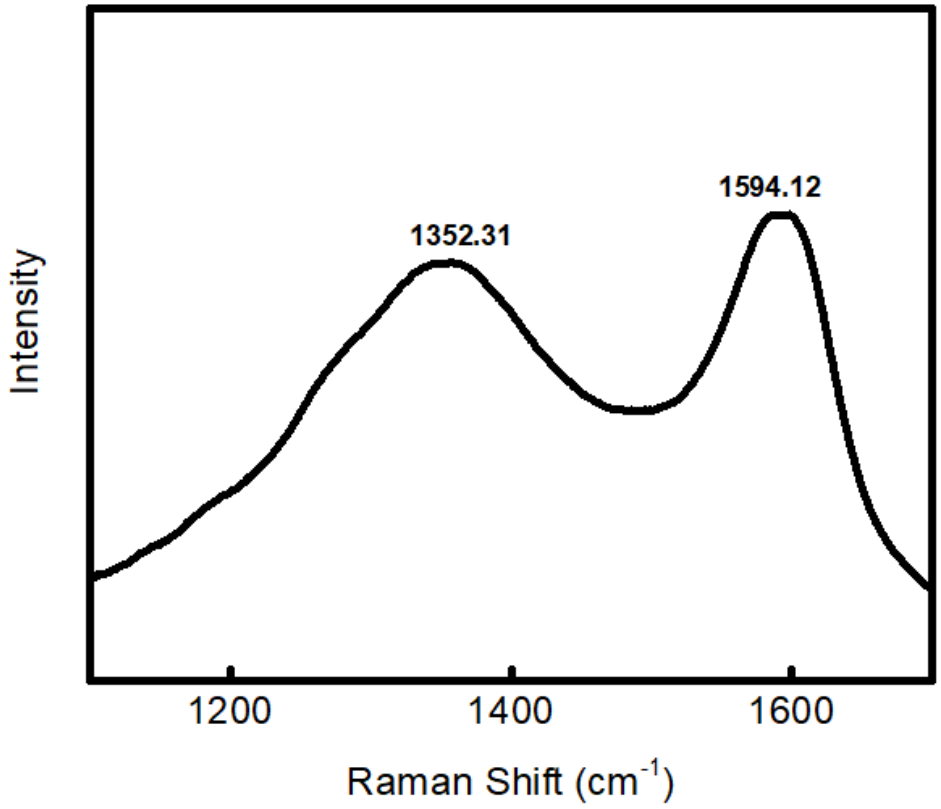

Figure 9: Raman spectra of C extracted from sugar

2.5.3 UV-Visible Spectroscopy. Figure 10 (a) is the UV visible transmittance spectroscopy data of ethanol, pure BTO, and carbon coated BTO. The pure BTO and carbon coated BTO were sonicated properly using ethanol before collecting UV-VIS spectra. As the ethanol is used, we considered UV-VIS spectra of ethanol as our reference. From the transmittance spectra in Figure 10 (a) it is quite clear that the intensity of ethanol is highest which means it transmits more light than pure BTO and Carbon coated BTO.

The carbon-coated nanoparticles transmit less amount of light as the carbon coating acts like a mask on the nanoparticles, and that's why the intensity of transmitted light is low in comparison to ethanol and pure BTO. Below Figure 10 (b) is the absorbance spectra of pure

BTO and BTO+C nanoparticles calculated by considering the transmittance of ethanol as reference. The absorbance spectra were calculated using the following equation:

$$A = log_{10}\left(\frac{i}{I}\right) \ldots\ldots\ldots\ldots (1)$$

Where A= Absorbance

i= Transmittance of ethanol and

I= Transmittance of BTO or carbon coated BTO

In figure 10 (b) the green-colored graph represents the plot of carbon-coated BTO vs ethanol and the black colored graph represents the plot of pure BTO vs ethanol. As BTO+C nanoparticles have low intensity in transmittance spectra, the absorbance spectra and the absorption coefficient value is high. While comparing two absorption spectra of BTO and BTO+C with each other, it can be easily found that the maximum peak position remains unchanged. This leads to the fact that the particle size remains more or less same.

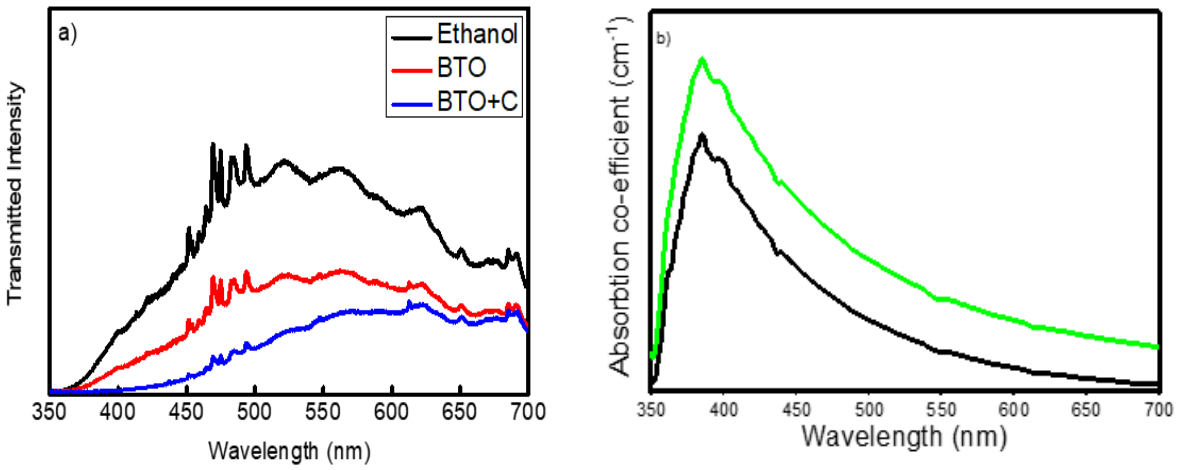

Figure 10: UV-VIS transmittance spectra (a) and absorption spectra of ethanol, BTO, and BTO+C (b)

From the absorbance spectra, it is visible that the absorbance is maximum when the transmittance is minimum, and it goes down to the minimum when the transmittance is maximum.

2.5.4 EDS. To explore the presence of prominent material in the synthesized sample EDX analysis was performed. EDX was also performed on pure BTO nanoparticles, and the EDX data of pure BTO nanoparticle was compared with the EDX data of synthesized carbon-coated BTO nanoparticles. The normalized EDX plots in Figure 11 (a) and (b) help evaluate the presence of carbon in pure BTO and BTO+C, these two EDX plots also confirm the presence of expected materials in the prepared CSNPs.

The comparison between Figure 11 (a) and (b) helps visualize the difference in intensities of carbon peaks present in pure BTO and in BTO+C CSNPs. It is quite clear that the intensity of carbon in pure BTO is much lower than the intensity of carbon in BTO+C nanoparticles. Figures 12 (a) and (b) represent the SEM images of pure BTO and BTO+C respectively. In these SEM images the particles are so agglomerated with each other that the grains of the particles are not clearly visible. So it is very hard to distinguish any change from these two SEM images. So it can be concluded that there is some possibility of carbon coating on the surface of BTO.

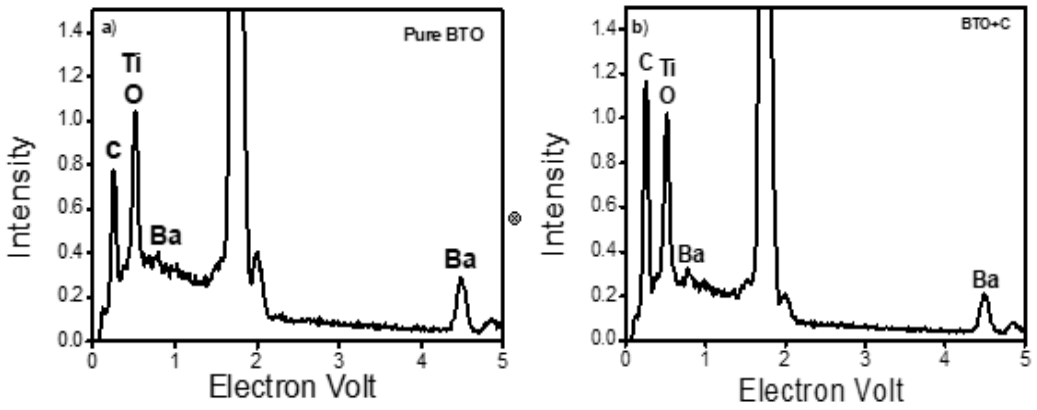

Figure 11: Normalize EDS plot of pure BTO (a) and BTO+C (b)

a) b)

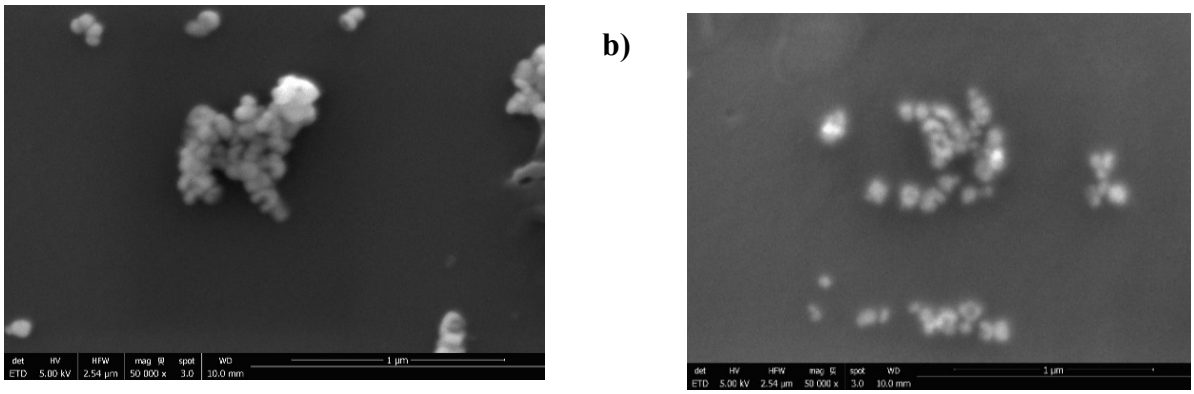

Figure 12: SEM images of pure BTO (a) and BTO+C (b)

2.6 Conclusions

In the present work, a unique physio-chemical method was implemented to develop carbon coated BTO nanoparticles. The obtained result from XRD analysis confirms the crystal structure of these CSNP and the presence of polycrystalinity. Among the other characterization methods, Raman characterization gives information about different vibration modes present in BTO and their interaction with Carbon. In Raman spectra, the peaks due to the presence of carbon are homogeneous to the graphite-like carbon structure. The comparison between the Raman spectra of carbon with the Raman spectra of glucose (after annealing) reveals Raman shift which may be due to the internal stress among the atoms. The occurrence of this internal stress may be due to carbon coating on the surface of BTO nanoparticles. UV visible spectroscopy reveals the fact that the absorbance peak increases with the instigation of carbon. The comparison of intensities of carbon, present in the EDX data of pure BTO and carbon-coated BTO reveals the presence of carbon in the synthesized core-shell nanoparticles. This surface topological analysis is conclusive evidence of the presence of carbon on the surface of BTO nanoparticles.

CHAPTER 3: SYNTHESIS AND CHARACTERIZATION OF CORE-SHELL NANOPARTICLES PREPARED BY PULSED LASER ABLATION

3.1 Abstract

In this paper CSNP with nitrogen doping in the shell region of the CSNP have been synthesized using pulsed laser deposition. One of the popular perovskite materials like BTO is used as a core material for the CSNP. Toluene and dimethyleformamide are used for carbon and nitrogen sources respectively. XRD and Raman characterization techniques are used to analyze the structural and vibrational characteristics. The reitveld analysis and TOPAS fitting of the raw XRD data reveal the intactness of crystal structure of BTO after carbon coating with nitrogen doping in the shell. In the Raman spectroscopy data all Raman active vibrational modes of BTO and carbon are present in the synthesized CSNP confirming the binding of carbon with BTO. Though nitrogen is not detected by Raman spectroscopy due to some limitations, SEM and EDX studies confirm the presence of prominent elements including Ba, Ti, O, C, and N in the synthesized CSNP the CSNP. TEM-EDS mapping and line scan confirm the presence and growth of carbon around the surface of BTO nanoparticles. Fluorescence spectroscopy also provides the information about the effect of nitrogen doping in the CSNP.

3.2 Introduction

The cubic perovskite structure (ABO_3) such BTO has excellent chemical and structural stability, which make them an attractive material in many research works. The main drawback of cubic perovskite materials is their bandgap. The bandgap of these materials is very large which is greater than 3.2eV. This high bandgap limits the use of perovskite materials in so many

applications. To reduce the bandgap so many metallic and non-metallic elements are incorporated with cubic perovskite materials. Many ongoing research works are based on the formation of heterojunction nanocomposites. These nanocomposites are a combination of low and high bandgap materials. In these heterojunction nanocomposites, the low bandgap materials are used to mitigate the effect of high bandgap materials. These low bandgap materials are usually doped at the surface of the high bandgap materials. Doping with other metallic or non-metallic elements induces defects, and these defects enhance the light absorption properties. Among these metallic and nonmetallic materials, nitrogen is the most popular element to reduce this large bandgap. The non-metallic doping element like nitrogen not only reduces bandgap but improves the carrier mobility[15]. Nitrogen enhances the carrier mobility as it has a long wave function of s/p electrons. There are many research works based on N_2 doping on perovskite materials, here we try to depict a work on N doping CSNP with BTO as a core material and nitrogen doped carbon as a shell material.

The carbon coating on BTO increases the biocompatible properties. Any kind of organic or inorganic, metallic or non-metallic elements can be doped on the surface of the nanoparticles. As carbon has a good binding property with any kind of material, it can be suitable with organic or inorganic and metallic and nonmetallic materials. The nitrogen doping on the carbon-coated surface helps generate a C-N bond. There are wide applications of the C-N bond[16]. They can be used in photovoltaic, catalytic, as well as biomedical applications. This C-N bond also has many memory applications. The biocompatible property of C makes a suitable element for different biomedical applications. The C-N bond also enhances the material's optical properties[17]. There are several studies based on nitrogen doping on various carbon materials. Nitrogen doped various carbon materials such as graphene, graphite, porous carbons, carbon

nanotubes, and nanofibers, and fullerenes have shown attractive improvement over the electronic and chemical properties of carbon. Graphene is one of the attractive carbon material, and there are many promising works based on nitrogen doped graphene. In recent years nitrogen doped graphene is used to enhance the performance of fuel cells and increase the performance of batteries. Pyridinic, pyrollic, and graphitic are the three types of N doped graphene. The Pyridinic graphene has a hexagonal crystal structure where the N atoms are bonded with two C atoms. In the pyrollic graphene the N atom is attached with two carbon atoms while it has a pentagonal crystal structure. In both the graphene structures the N atom is attached at the edge of the layer[18]. There are possibilities that this N atom can be present at the inside of the layer to fulfill other vacancies. In the graphitic graphene, the N atom substitutes one of the carbon atoms and makes the bond with three carbon atoms. These carbon atoms are in sp^2, and this kind of N attachment occurs inside the layer[19]. So many configurations are possible with N doping on carbon materials. N atom doping provides different crystal structures that are useful to improve the physical, mechanical, and chemical properties of different carbon materials. The improvement of the properties of materials combining N and C atoms are the main motivating factor in this research.

In our present work, we used the pulsed laser ablation technique for carbon coating and nitrogen doping. Toluene and Dimethylformamide (DMF) were used as the carbon and nitrogen source. Leaser shots were used to break the atomic bonds in Toluene and DMF. The DMF acts as the nitrogen source, and here the nitrogen is a doping element so the amount of DMF is lower than Toluene. In DMF the nitrogen atoms create a single bond with the methyl group. This single bond can be easily breakable with leaser shots, so the extraction of nitrogen would be easy in DMF. In toluene one methyl group is attached with a benzene ring. As the methyl group has a

single bond with benzene it can be detached easily using UV laser. This methyl group will act as a carbon source, and it will nucleate over the surface of $_{BTO}$. The BTO has a very compact crystal structure it does not have voids at its surface. So Carbon or nitrogen can only nucleate at the surface of BTO. Some possible facts arise with this synthesis technique. Mainly there are four possibilities: first is the BTO particles may agglomerate with each other, second is some of the BTO particles are coated with carbon and some of them remain uncoated, third is the carbon and nitrogen particles may agglomerate with each other, the last one is some of the BTO particles may partially be coated and nitrogen-doped. To eliminate other possibilities and to confirm nitrogen doping we performed some characterization, and they are mainly XRD, Raman spectroscopy, SEM, and fluorescence spectroscopy. In this research work, we have tried to establish the presence of nitrogen doping in BTO based CSNP.

3.3 Synthesis Procedure

3.3.1 Materials. Pure BTO nanoparticles, Toluene, and Dimethylformamide (DMF) were the primary materials. Toluene was used as the carbon source to create the shell over BTO nanoparticles. Dimethylformamide (DMF) was used as the nitrogen source for nitrogen doping. Acetone (C_3H_6O), ethanol (C_2H_5OH), and deionized water are used as the secondary materials in this laser ablation process. The BTO nanoparticles with a particle size of 50nm and purity of 99.95% were bought from Inframet Advanced Materials, USA. Toluene and DMF with a purity of 99.9% were brought from Fisher Chemicals.

3.3.2 Procedure. Pure BTO nanoparticles (17.2 mg) were mixed with toluene (20ml) and DMF (5ml). To disperse the particles, the solution was placed under a probe sonicator for 1 hr. A laser was used as the energy source to break the atomic bonds in toluene and DMF. The Laser

was made by Quantel, power 1100VA, voltage 100-240 V, AC frequency- 50/60 Hz, the pulse width of the laser lamp was 170 microsecond. The solution of BTO+Toluene+DMF was placed in such a way that the laser pulses could hit the solution directly. During this laser hitting process, the solution was kept over a bath sonicator. The bath sonicator prevented the particles to precipitate at the bottom of the cuvette. The number of laser shots was 20,000-25,000, which took approximately half an hour. These laser shots break the atomic bond in toluene and DMF, and it also produced sufficient energy to generate carbon coating and nitrogen doping over the surface of BTO nanoparticles.

3.3.3 Removal of Contamination. The separation of particles from the solution was done by the centrifugation procedure. After laser ablation, the solution was placed inside a centrifuge for 10-15 min at 800 rpm. This helped to separate nanoparticles from the liquid solution. The next step was the removal of contamination which was carried out by ethanol and acetone wash. The mixture of ethanol acetone and particle was placed over a hot plate for 10 minute. After 10minutes the alcohol evaporated and the particles were extracted by spatula and kept in tubes for characterization. The below Figure 13 is the schematic diagram of synthesis procedure provides all steps of the synthesis using pulsed laser ablation.

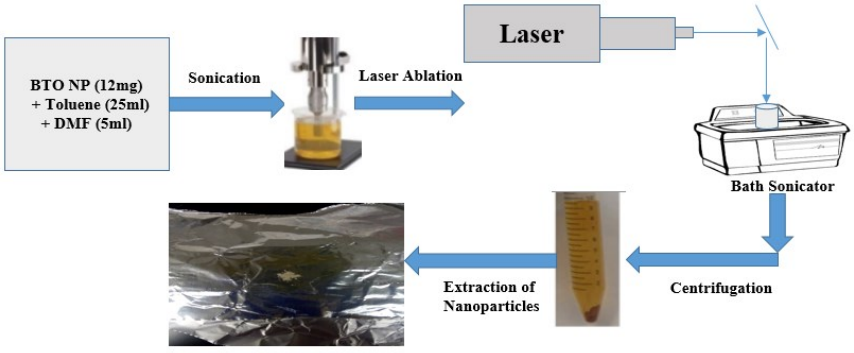

Figure 13: Schematic diagram of synthesis procedure with laser ablation technology

3.4 Characterization

All the samples were characterized by using XRD (Brucker, D8 Discover) to get some information about its diffraction patterns. The θ-2θ scan was done with CuK_α (λ=1.5405 angstrom). The Reitveld refinements were executed by Diffrac^{plus} TOPAS software. Raman Spectroscopy was carried out to gain information about the vibrational modes. The Raman Spectroscopy was analyzed by NSG Lab spec software. Surface topological analysis was carried out by SEM, and confirmation of elements was done by EDX. Fluorescence spectra collected to see the luminescence properties and the effect of N doping on luminescence properties.

3.5 Results and Discussion

3.5.1 XRD. XRD is a nondestructive characterization technique which is used to determine the chemical composition and crystal structure of a natural or laboratory manufactured materials. Figures 14 (a) and (b) represent the X-Ray diffraction pattern of N doped BTO-C CSNP and pure BTO. Both X-ray diffraction patterns are fitted with TOPAS software. In these two figures the black, red, and blue line represents the observed, calculated, and difference values. For pure BTO the diffraction peaks are present at $2\theta = 21.75^0$, 31.35^0, 38.42^0, 44.89^0, 50.64^0, 55.80^0, 65.52^0, 70.07^0, 74.62^0 and 78.94^0. To determine the crystal structure of pure BTO Reitveld refinement analysis was used. At first, all the possible crystal structures of BTO were collected from the crystallographic open database, and these data were uploaded with the raw XRD data of pure BTO into TOPAS software. In TOPAS software there were several parameters like instrument details, background, correction, miscellaneous, etc. These parameters play a vital role to get accurate and error-free results. The second step in this fitting process was putting accurate values of these parameters in TOPAS software. The background value was kept as 8

which denotes the order of the polynomial equation. The goodness of fit value or GOF value determines the accuracy in this fitting process. The final step was the fitting, and cif file was quite matched with the raw data. The goodness of fit value was 1.14 which indicates the accuracy of the fitting. The weight percentage after fitting was the conclusive evidence of the crystal structure of pure BTO which was tetragonal and matched with P4mm space symmetry. The next step was the fitting of N doped BTO-C CSNP, and fitting was done using three different cif files of BTO, C, and N. As the BTO had a coating of carbon at its surface that's why the cif file of C was used. To determine the N doping effect on this carbon coated nanoparticles cif file of N was used. Figure 14 (b) represents the fitted data of C coated and N doped BTO. This data quite resembles with XRD of pure BTO. The peak positions in Figure 14 (a) matches with the peak positions in Figure 14 (b). In C coated N doped BTO the intensities of the peaks are lower than the intensities of the peaks in pure BTO. The reason behind this is that C coating may act as a mask on the BTO nanoparticles that's why the intensities of the peaks are decreased. The bond angles and bond length remained quite same with fitted BTO data. The weight percentage after fitting gave the information that the peaks of carbon-coated and nitrogen-doped BTO had a higher percentage of matching with the cif file of BTO. The weight percentage of carbon and N had a minimal amount of percentage matching. To get some conclusive evidence from XRD data calculation of crystal size was done with the help of sheerer equation, which is

$$\tau = \frac{K\lambda}{\beta cos\theta}$$

Where,

τ= crystallite size

K= dimensionless shape factor, its value is close to unity i.e. 0.9

B= Full-width half max θ= Bragg angle

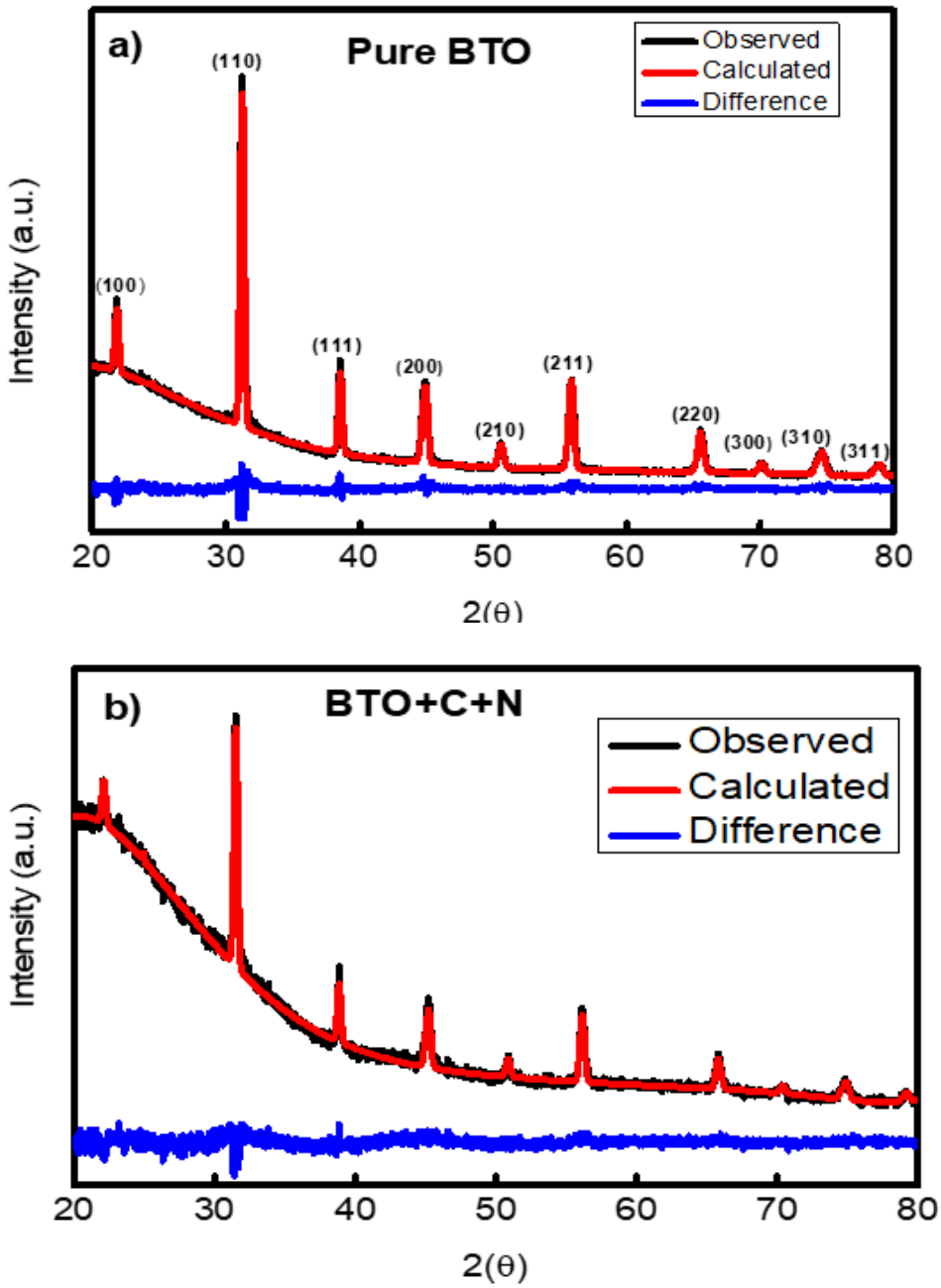

Figure 14: Fitted and raw XRD data of pure BTO (a) and BTO+C+N (b)

The crystal size of pure BTO was 19.3 nm while the crystal size of carbon-coated and N doped BTO was 20.6nm. It can be concluded from the calculated crystal structure that nitrogen may present at the shell as a doped material and there is no epitaxial growth of nitrogen around the shell of carbon.

3.5.2 Raman Spectroscopy. The Raman spectra for carbon coated CSNP with nitrogen doping in the shells are presented in below Figure 15. In the unit cell structure of BTO, it has five atoms and fifteen degrees of freedom per unit cell. The cubic phase of BTO has O_h symmetry. The fifteen degrees of freedom are divided by optical and acoustical branches. The optical branch is represented by $\mathbf{3}\boldsymbol{F}_{1u} + \boldsymbol{F}_{2u}$ Raman modes, and the acoustical branch is represented by $\boldsymbol{F}_{1u}$ Raman mode. The $\boldsymbol{C}_{4u}$ symmetry is present in BTO which has a tetragonal crystal structure. The tetragonal BTO has Raman active modes which are represented by 4E (TO+LO) + $3A_1$ (TO+LO) + B_1 (TO+LO).

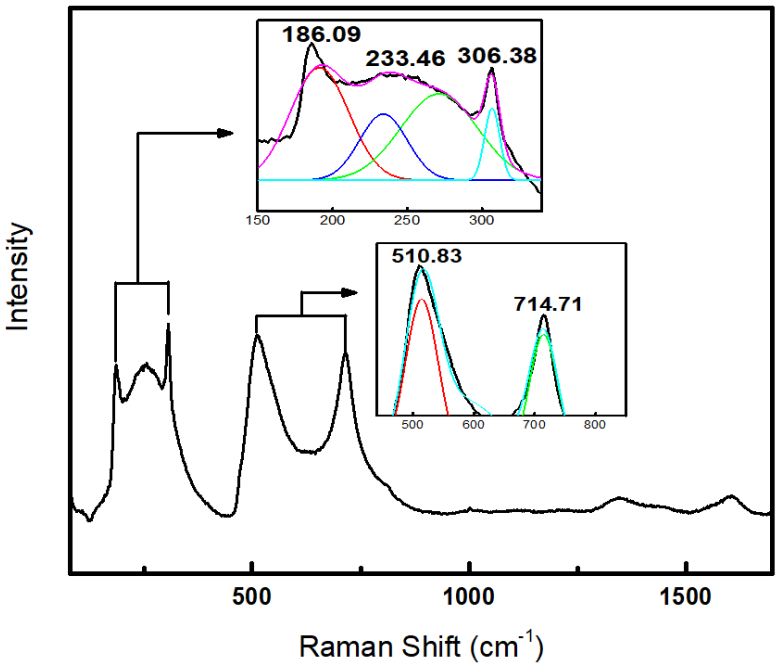

Figure 15: Raman spectra of BTO+C (BTO Raman peaks are zoomed in)

These data are for tetragonal BTO having space group symmetry (P_{4mm}). In Figure 15 the frequency range was covered from 100 cm^{-1} to 2000 cm^{-1} with the laser excitation wavelength of 532nm. In this Figure, we mainly emphasize on Raman peaks associated with BTO. The BTO peaks are also deconvoluted and zoomed in a single origin plot to clear the visibility. The Raman spectra of pure BTO and Carbon coated BTO are depicted in below Figure 16. In this Figure, the red line indicates Raman spectra of carbon-coated BTO and the black colored graph represents pure BTO nanoparticles. The frequencies near to 190, 250, 303, 512, and 715 cm^{-1} are associated with different Raman modes of pure BTO.

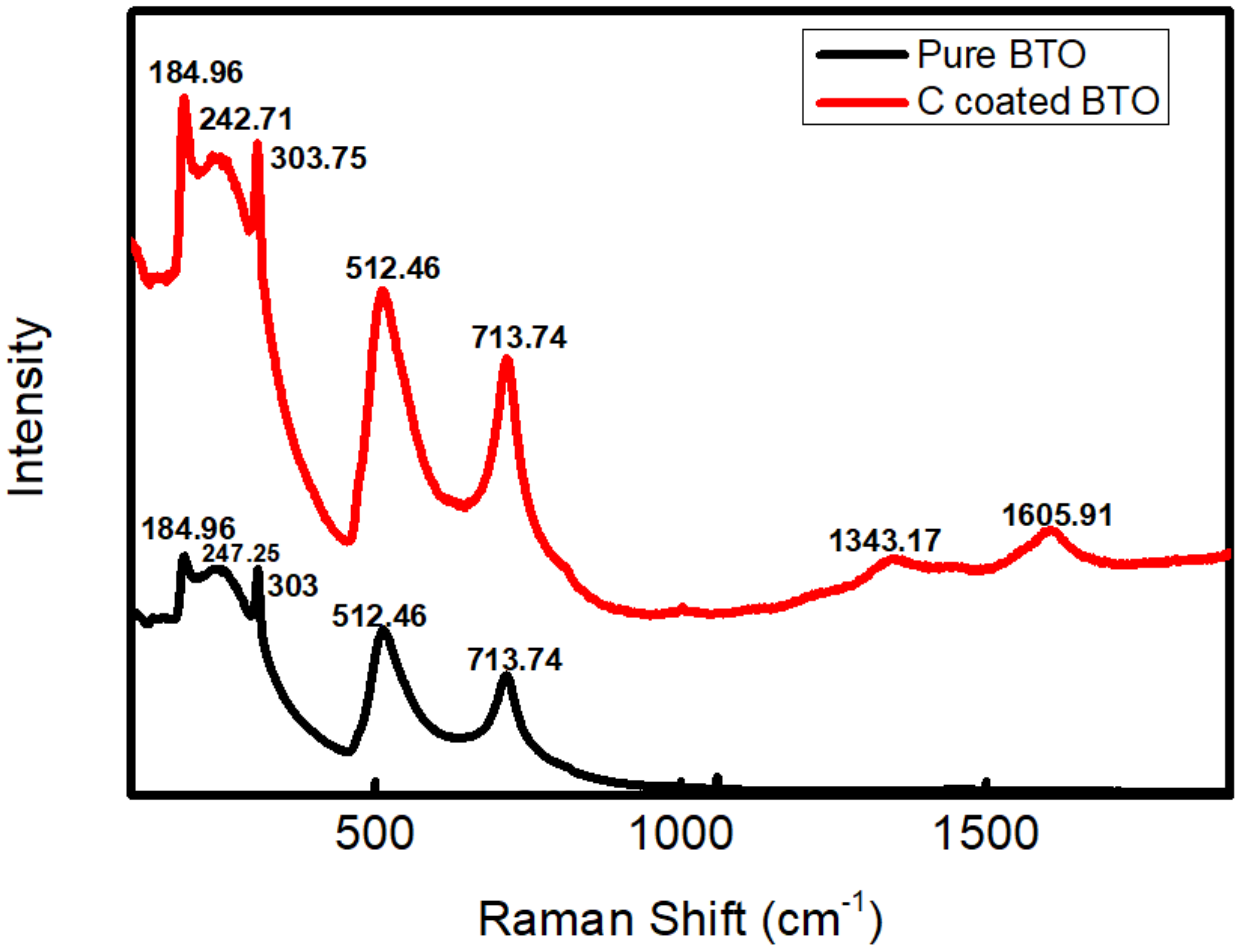

Figure 16: Comparison between Raman plot of Pure BTO and BTO+C

It is quite clear from the Raman spectroscopy data that all Raman modes for pure BTO are present in the Raman spectra of carbon-coated BTO. So it can be concluded that the BTO peaks are well intact with carbon peaks. According to the literature, the three ***E*** (TO) Raman modes of BTO are presented by the frequencies near 190, 280, and 516 cm^{-1}. The frequencies near 303 and 720 cm^{-1} represent the ***E*** (LO) Raman modes[20]. The occurrence of internal stress due to carbon coating on BTO nanoparticles results Raman shift. Below Figure 17 is the Raman spectra of BTO@C core-shell nanocomposites, and this portion mainly emphasize the Raman active modes of carbon. The peaks associated with carbon are deconvoluted and zoomed into the plot for improvement of the visibility of peaks and reduction of multiplicity.

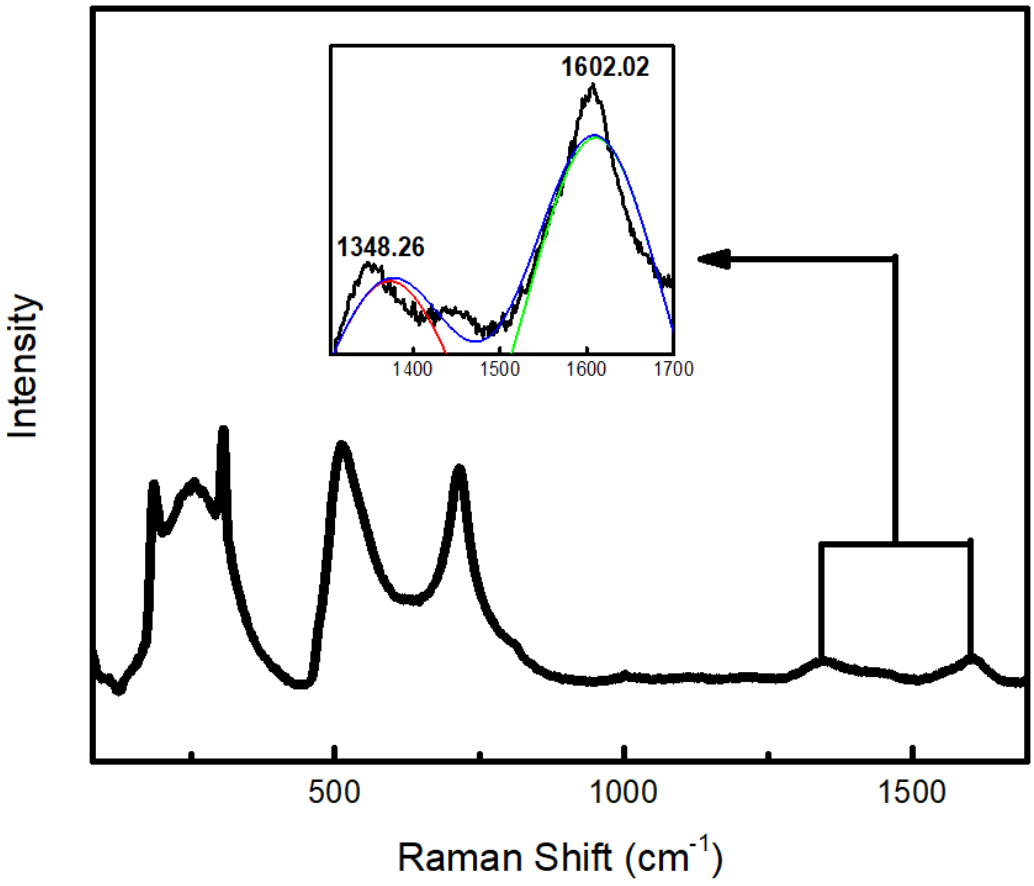

Figure 17: Raman spectra of BTO+C (carbon Raman peaks are zoomed in)

In the carbon portion, there are two main visible peaks at frequencies 1348.26 and 1602.02 cm^{-1}. These two peaks are named D band and G band respectively. The presence of these two peaks matches with amorphous carbon. The nature of crystallinity depends on the sharpness and broadness of the D band and G band. As these two vibrational peaks are broad, it indicates poor crystallinity in the as-formed state. According to the literature, the in-plane termination of disordered graphite generates vibrations in carbon atoms. These carbon atoms vibrate with a dangling bond. This is the main reason for the D band peak at around 1348 cm^{-1}. The peak at 1602.02cm^{-1} (G band) is due to the vibration among the sp^2 bonded carbon atoms. From the analysis, we cannot tell about the formation of a core-shell structure, but we can confirm the presence of carbon and its intactness with BTO. Unfortunately, we could not detect any vibrational mode associated with CN due to some instrumental limitations.

3.5.3 SEM and EDS. The surface topological analysis was done by SEM, and the elemental compositional analysis by EDS. Below Figure 18 is the normalized EDX plot of carbon coated and nitrogen-doped nanoparticles. The presence of Ba, Ti, N, and C is quite clear from this EDX data. According to the EDS energy table, N has characteristics of X-ray energy at 0.392 keV. Similarly, Ti and O both have characteristics of X-ray energy at 0.452 keV and 0.525 keV, respectively. It is quite clear from the EDS energy table that the characteristic X-ray energy of N, Ti, and O is very close to each other. So there is a chance that the peaks of N may be covered by the peaks of Ti and O. Here the nitrogen is the doping element so the amount of N in the synthesized CSNPs is lower than other elements. To mitigate the visibility problem of N we zoomed in to the EDS data and highlighted the N portion. In the zoomed in portion of this EDS plot, it is quite clear that there is an unknown peak present near Ti, and the position of that particular peak matches with the characteristics X-ray energy of N. So it can be concluded that

this peak is associated with N. This line-scan data also reveals the presence of N in the sample. Below Figure 19 is the origin plot of the line scan and the below image represents the corresponding SEM image of the line scan. In the origin plot of line scan the green, the red, pink, blue and black line represents Ba, C, Ti, O and N. At the middle of this line scan the maximum signal is from the core elements i.e. Ba, Ti, and O. So at the middle portion of the line scan the intensity of C is lower than the core elements.

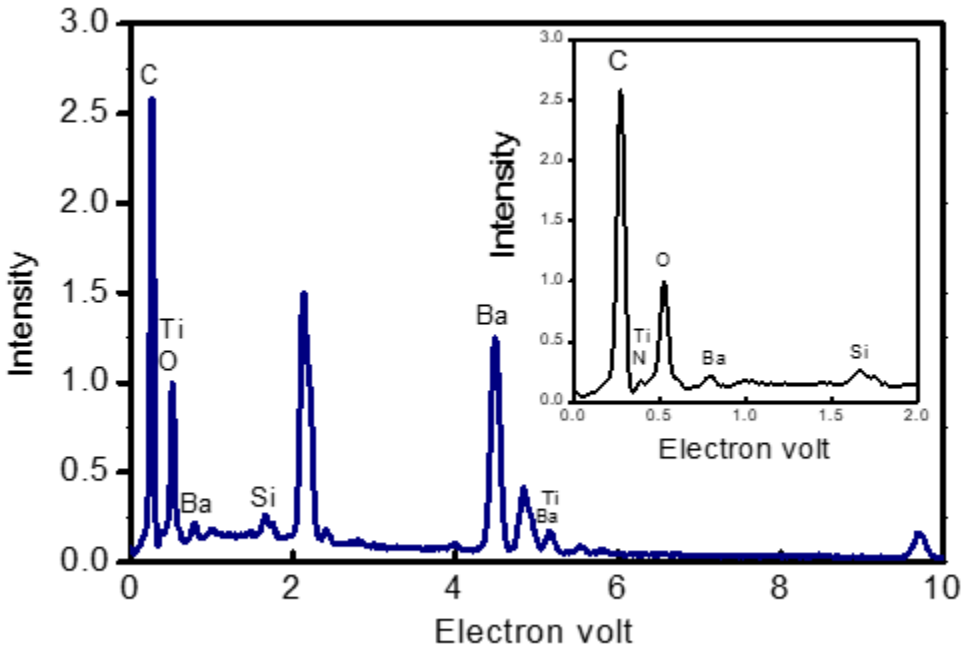

Figure 18: Normalized EDS plot of BTO+C+N

At the end portion of the line scan, the maximum signal is from the shell element as carbon is the shell material so the intensity peaks from core elements are lower than carbon. As nitrogen is the doped element and its amount is lesser than other materials, the intensity of nitrogen is low throughout this line scan data. The presence of nitrogen is not conclusive with

this line scan data so the mapping of SEM images for each element was conducted to provide some definite evidence about the presence of nitrogen. Below Figure 20 represents the mapping of SEM images. Before taking SEM images the nitrogen doped CSNPs were sonicated properly and placed over silicon substrate. The sonicated particles and the silicon substrate were placed over an Al disk and attached with carbon tape. As we used silicon substrate that's why there is a SEM mapping image of silicon.

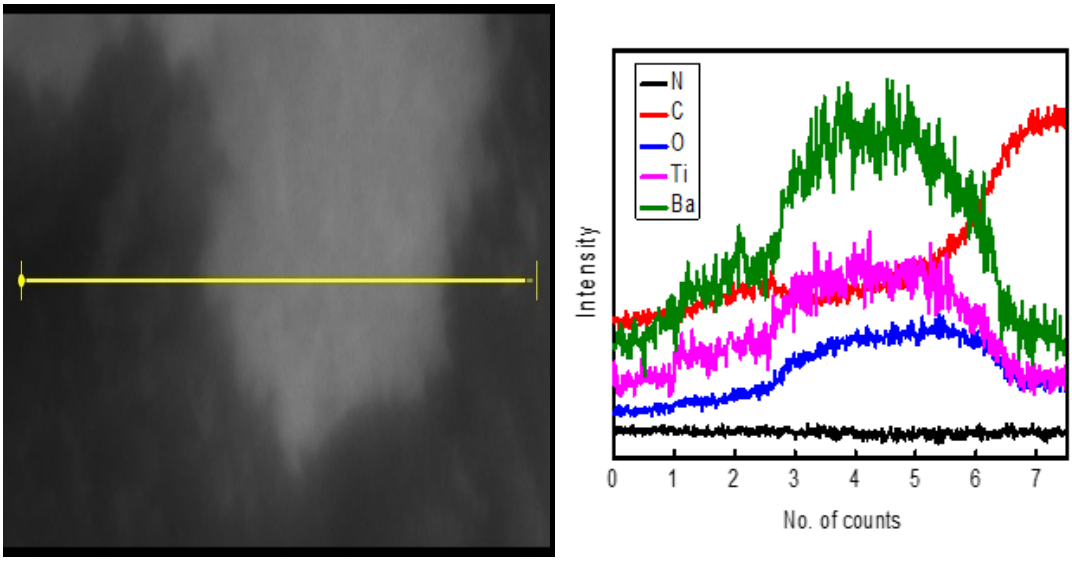

Figure 19: Line scan of BTO+C+N

The SEM mapping images follow the surface topology. This proves the presence of nitrogen in the synthesized nanoparticles. The mapping SEM image of nitrogen also follows the surface topology like other elements. But this is not a definite conclusive evidence as mapping of SEM image of pure BTO also reveals the presence of nitrogen. The possibility of such a confusing result can be explained by the position of nitrogen and titanium. The position of these two elements are very close that's why SEM might detect both of them.

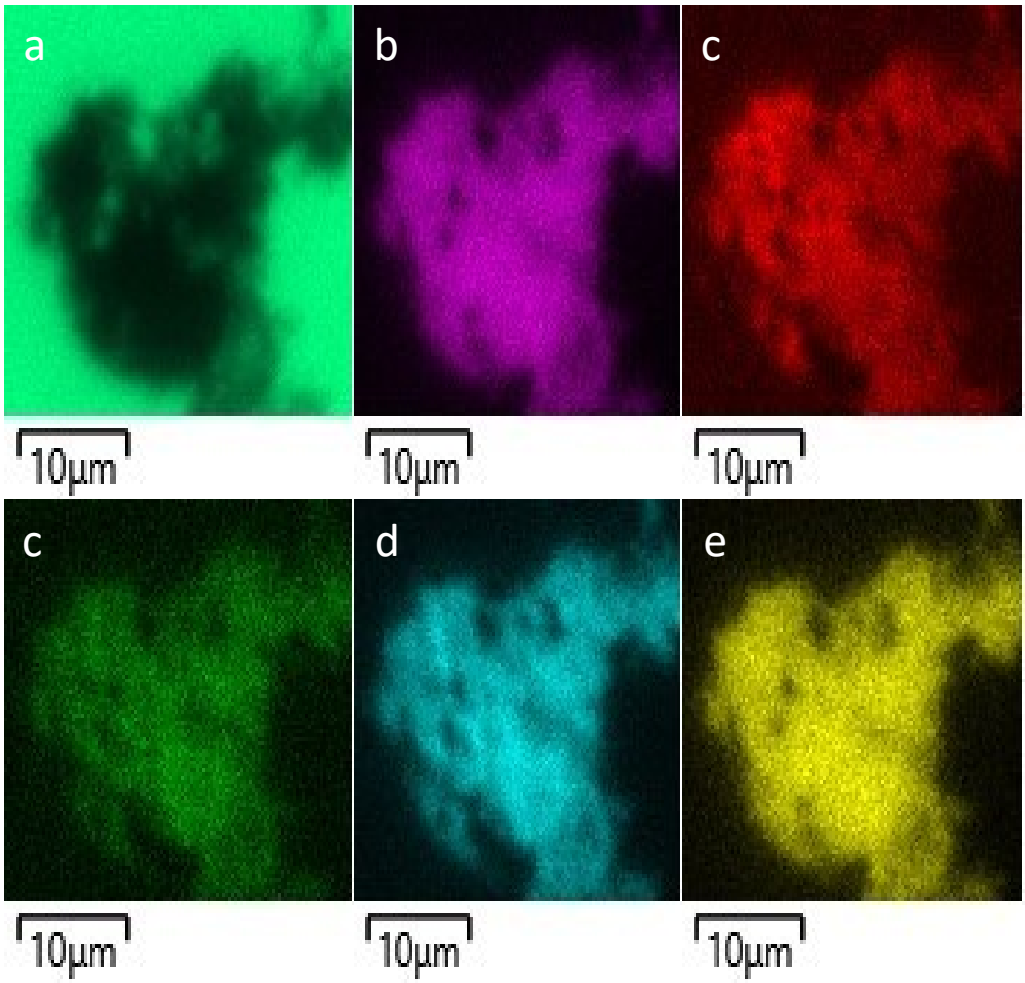

Figure 20: SEM mapping images of a Si, b Ba, c C, d N, e O and f Ti

3.5.4 TEM. Below Figure 21 show the transmission electron microscopy images of oxygen, titanium, barium, and carbon. These images are very helpful to find the growth pattern of different elements. The TEM image of carbon reveals that the carbon nucleates around the surface of the BTO nanoparticles. Where the blue, yellow, red and sky blue TEM images represents O, Ti, Ba and C respectively.

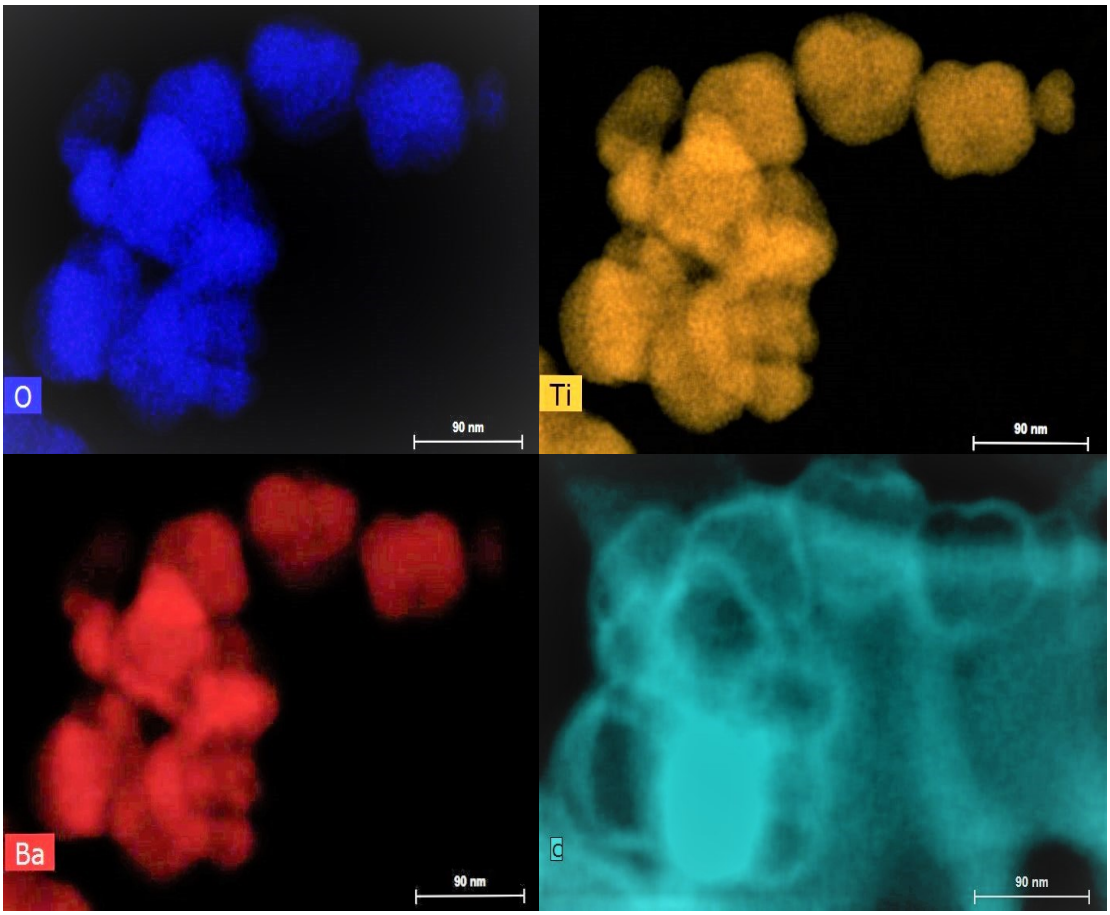

Figure 21: TEM images of oxygen, titanium, barium, and carbon

Below Figure 22 shows the TEM and the line scan images of two nanoparticles which are agglomerates with each other. In the line scan, different line colors are associated with different elements. The carbon is represented by the green line. In the CSNP, the shell element is carbon that means carbon is located at the surface of these nanoparticles. In the line scan, it is quite obvious that at the surface the signal is from the carbon so the intensity of carbon is high in comparison to the intensity from core elements.

Inside the core, the intensity from the core elements is higher than the intensity of shell material i.e. carbon so the magnitude of the green line is low. Now at the point where the two particles are connected with each other, the intensity count of the carbon (green line) is higher

than other core elements. As these two particles are agglomerates with each other so the surface of these two particles is interconnected which is the main cause of this high intensity of carbon. The line scan can be a possible evidence for presence of shell element which is carbon, and the line scan is conclusive evidence of the formation of core-shell nanoparticles.

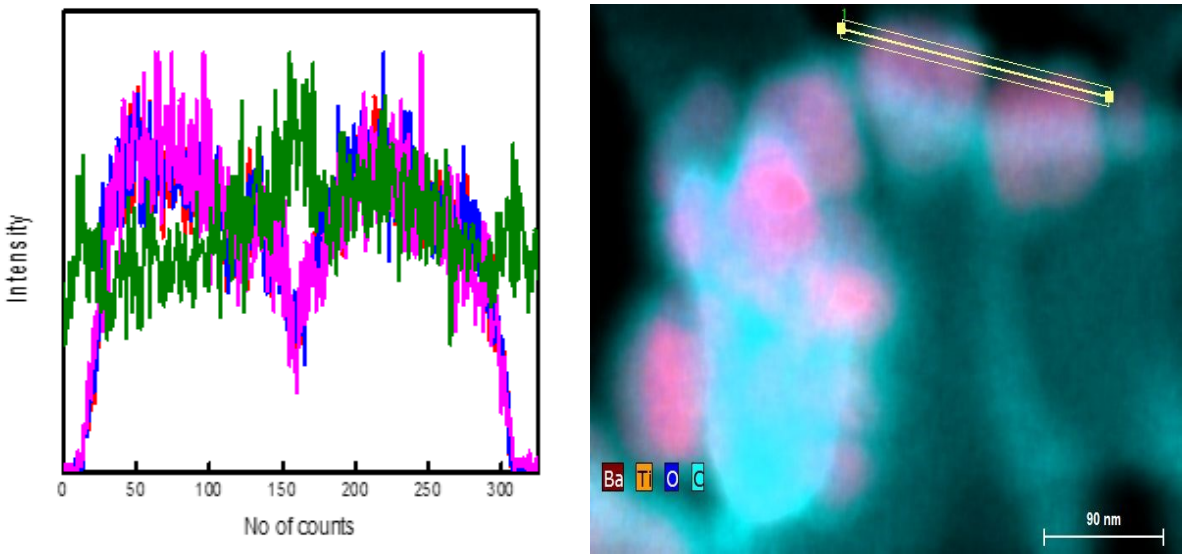

Figure 22: Line Scan and TEM image of BTO+C

The line scan on the single-particle also follows the same pattern that is at the surface the intensity of the shell element is higher than the core elements, and inside the core, this pattern is reversed. In the TEM image, the red color is associated with BTO, and the bluish color is associated with carbon. From Figure 23, it is quite clear that carbon particles nucleate around the surface of BTO nanoparticles.

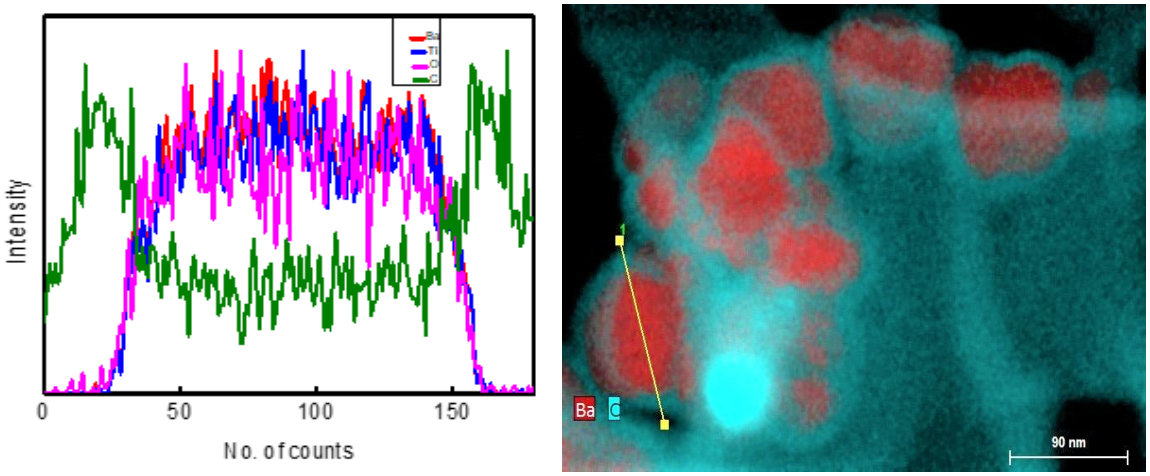

Figure 23: Line scan and TEM image of a single particle

3.5.5 Fluorescence Spectroscopy. Fluorescence spectra and Raman shifts were carried out to explore the optical properties of the CSNP. Before capturing the fluorescence spectra three samples (Pure BTO, BTO@C, and BTO@C+N) were sonicated properly inside DI water. Below Figure 24 is the Raman emission spectra of DI water with the excitation wavelength of 350 nm. Different excitation wavelengths were used to study the peak shift in emission spectra corresponding to its Raman shift[18]. To calculate the peak position of the emission spectra the following equation is used

$$\Delta\tilde{\nu} = \left(\frac{1}{\lambda_0} - \frac{1}{\lambda_1}\right)$$

Where,

$\Delta v = Raman\ shift$

λ_0 = Excitation wavelength

λ = Emission wavelength

Figure 25 displays the fluorescence spectra of nitrogen-doped carbon-coated BTO, where the portion of 620-640 nm is due to the Raman shift of carbon[21]. The corresponding emission peaks are calculated by using the above equation. From below Figure 25 it is clear that the emission spectra corresponding to the Raman shift of carbon changes its position with different excitations. In Raman spectra carbon has two genuine peaks one is due to the in-plane vibration of SP2 bonded carbon atoms named as G band and the other one is due to the out of plane vibration named as D band. The emission spectra for the G band are quite visible, and the spectra shift with different excitation wavelengths. This is one of the conclusive evidence of the presence of carbon in the as-synthesized nanoparticles. From below Figure 26 it can be observed that under different excitation the nitrogen-doped nanoparticles exhibit fluorescence spectra. In Figure 26 the portion around 660-720 nm corresponds to the fluorescence of nitrogen-doped nanoparticles. This fluorescence part is present due to the doping effect of nitrogen. In below Figure 27 it is quite prominently observable that a sharp peak is present in the higher emission wavelength. This sharp emission peak is also shifted position with different excitation wavelengths. This peak is due to the structural defects present on the surface of BTO. With the incorporation with other functional elements the intensity of this emission peak increases. In Figure 27 the black, red, blue and pink plots represent the fluorescence spectra of DI water, pure BTO, BTO+C and BTO+C+N, respectively. It is quite visible from the figure that the intensity of DI water gets amplified with BTO, and it increases more with incorporation of different functional groups like carbon and nitrogen.

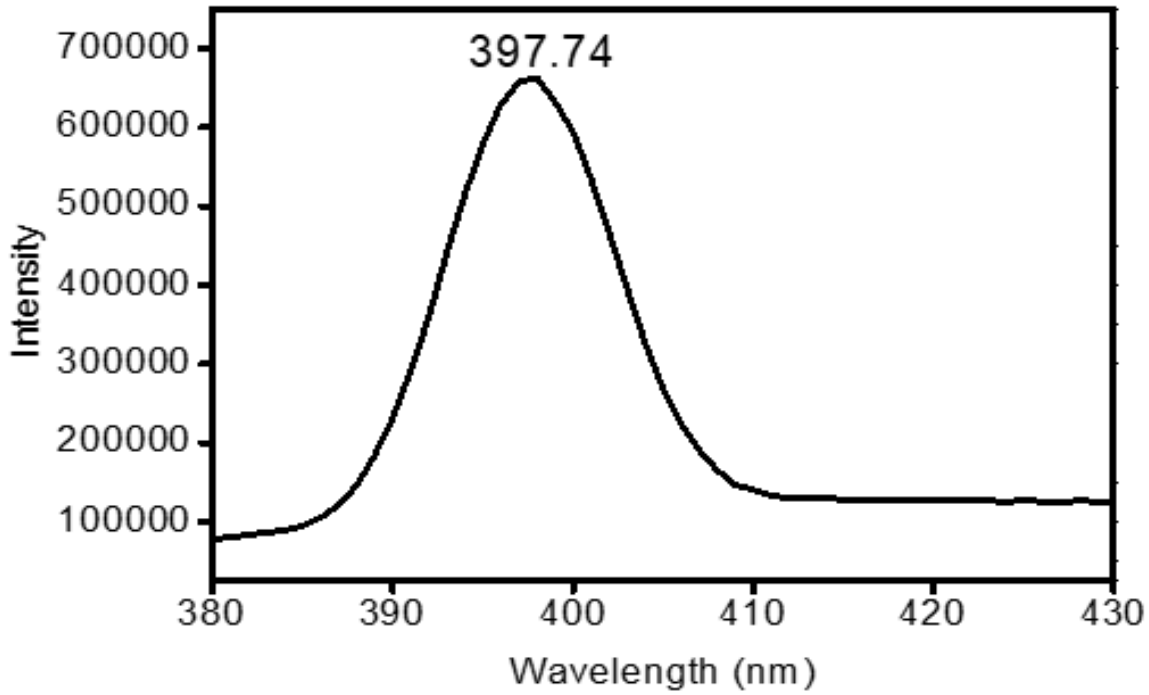

Figure 24: Raman spectra of DI water

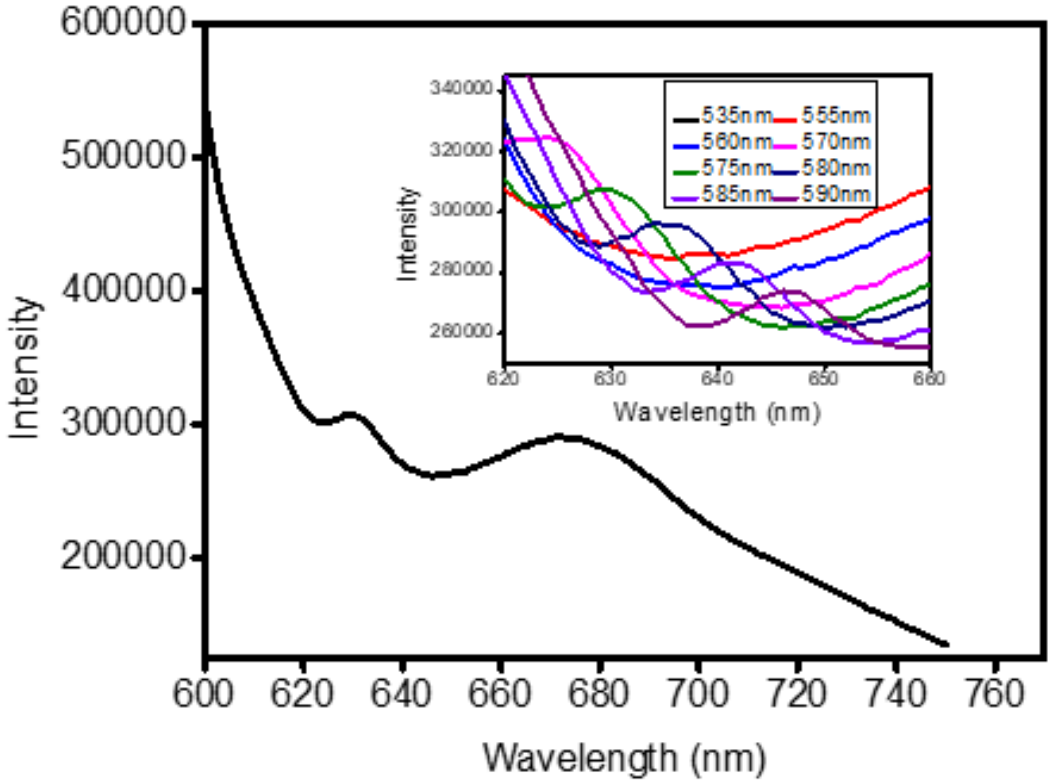

Figure 25: Fluorescence spectra and Raman Shift of carbon

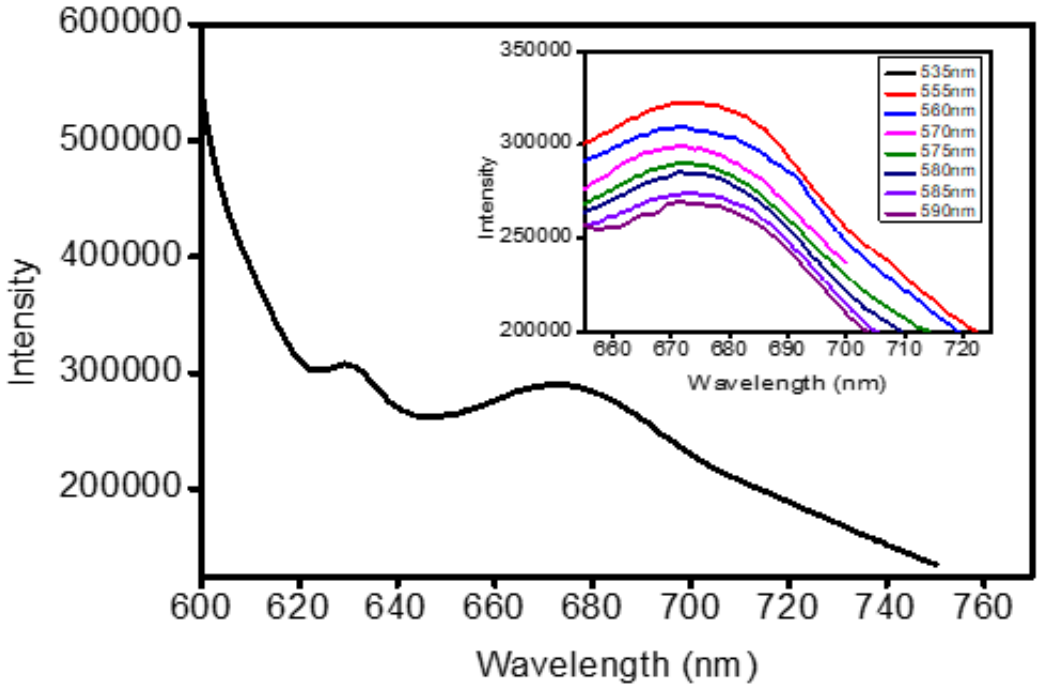

Figure 26: Fluorescence spectra for different excitations

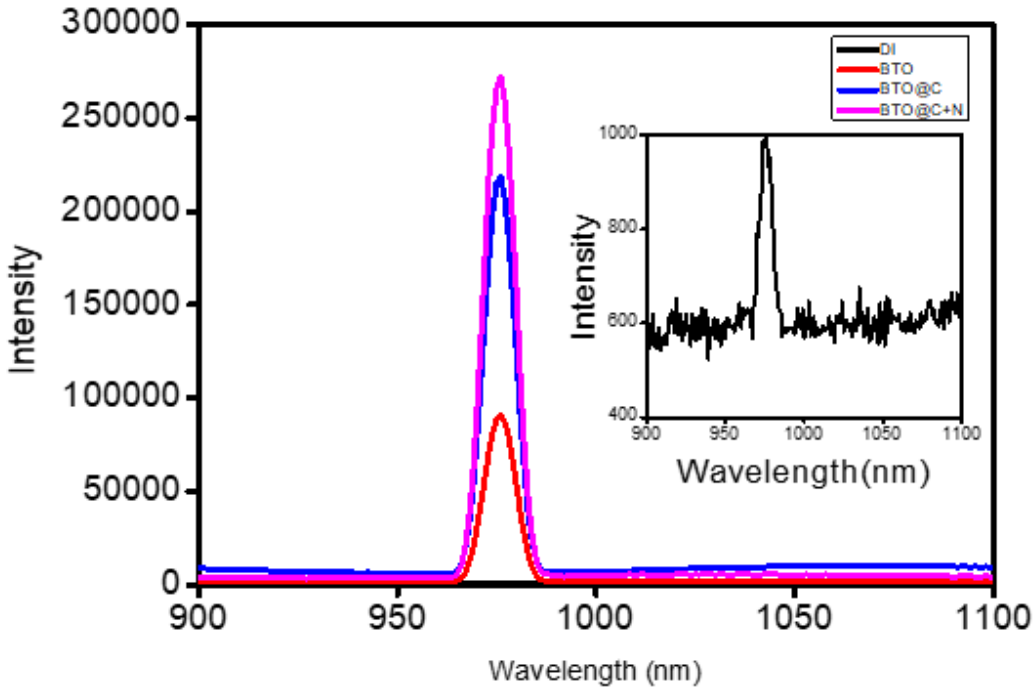

Figure 27: Comparison of fluorescence spectra of DI water, pure BTO, BTO+C and BTO+C+N

3.6 Conclusions

Synthesis of core-shell nanoparticle and nitrogen doping on the synthesized core-shell nanoparticle were successfully performed by pulsed laser ablation. The Rietveld comparison between the crystal structure of pure BTO and nitrogen-doped carbon-coated BTO bestowed that the crystal structure for pure BTO remained intact after carbon coating and nitrogen doping. Different Raman vibration modes associated with pure BTO are present in the prepared sample. The Raman peaks that are associated with carbon are also present in this synthesized nanoparticles. This Raman spectroscopic data also reveal the fact that carbon is showing good binding quality with BTO. The Raman shift indicates that there is some internal stress among the atoms due to carbon coating. The TEM data and line scan of TEM corroborate the formation of core-shell nanoparticles. The SEM images and EDX data justified the presence of nitrogen in the synthesized sample. The fluorescence properties increase with the incorporation of different functional groups, these functional groups may be Ammonia, Hydroxides, or cyanides. The fluorescence spectra due to the surface defects increase with nitrogen doping this phenomenon can be useful for various detection applications.

CHAPTER 4: CONCLUSIONS

The carbon-coated BTO, CSNP have been synthesized successfully with sonochemical and pulsed laser ablation techniques. One of the popular nonmetals like nitrogen is doped on the shell of the CSNP with the same pulsed laser ablation technique. The comparison between XRD data of pure BTO with the XRD data of CSNPs helps determine the actual crystal structure of CSNPs and pure BTO. XRD analysis also divulges the information about the unaltered crystal structure of BTO after carbon coating. Raman spectroscopy data provide information regarding the vibrational modes present in the synthesized CSNP. The Raman modes associated with core BTO and shell carbon are clearly visible in CSNP prepared using both techniques. The SEM, EDX, and TEM results show the presence of prominent elements in these CSNPs. TEM confirms the growth of carbon around the surface of BTO. The fluorescence spectra show changes due to nitrogen doping. The absence of nitrogen in Raman spectroscopy is solved by fluorescence spectra. The changes in fluorescence properties due to the incorporation of different functional groups may lead to the enhancement of the optical properties of these CSNPs. These improvements in optical properties will make these synthesized CSNP useful in many Nano-bio applications.

REFERENCES

[1] M. H. Frey and D. A. Payne, "Grain-size effect on structure and phase transformations for barium titanate," *Phys. Rev. B*, vol. 54, no. 5, pp. 3158–3168, 1996.

[2] R. Ashiri, A. Nemati, M. Sasani Ghamsari, S. Sanjabi, and M. Aalipour, "A modified method for barium titanate nanoparticles synthesis," *Mater. Res. Bull.*, vol. 46, no. 12, pp. 2291–2295, 2011.

[3] G. Wang, X. Chen, Y. Duan, and S. Liu, "Electromagnetic properties of carbon black and barium titanate composite materials," *J. Alloys Compd.*, vol. 454, no. 1–2, pp. 340–346, A 2008.

[4] K. Olurode, G. M. Neelgund, A. Oki, and Z. Luo, "A facile hydrothermal approach for construction of carbon coating on TiO2 nanoparticles," *Spectrochim. Acta Part A Mol. Biomol. Spectrosc.*, vol. 89, pp. 333–336, 2012.

[5] Y. H. Cheng *et al.*, "Raman spectroscopy of carbon nitride films deposited using the filtered cathodic vacuum-arc technique combined with a radio-frequency nitrogen-ion beam," *Appl. Phys. A Mater. Sci. Process.*, vol. 73, no. 3, pp. 341–345, 2001.

[6] Z. Zafar *et al.*, "Evolution of Raman spectra in nitrogen doped graphene," *Carbon N. Y.*, vol. 61, pp. 57–62, 2013.

[7] Z.-L. Zhang *et al.*, "Enhancement of Perovskite Solar Cells Efficiency using N-Doped TiO2 Nanorod Arrays as Electron Transfer Layer," *Nanoscale Res. Lett.*, vol. 12, no. 1, p. 43, 2017.

[8] Y. Shen, Y. H. Lin, and C.-W. Nan, "Interfacial Effect on Dielectric Properties of Polymer Nanocomposites Filled with Core/Shell-Structured Particles," *Adv. Funct. Mater.*, vol. 17, no. 14, pp. 2405–2410, 2007.

[9] J. Q. Qi, Y. Wang, W. P. Chen, L. T. Li, and H. L. W. Chan, "Perovskite barium zirconate titanate nanoparticles directly synthesized from solutions," *J. Nanoparticle Res.*, vol. 8, no. 6, pp. 959–963, Dec. 2006, doi: 10.1007/s11051-006-9069-6.

[10] S. Ram, A. Jana, and T. K. Kundu, "Ferroelectric BaTiO3 phase of orthorhombic crystal structure contained in nanoparticles," *J. Appl. Phys.*, vol. 102, no. 5, p. 054107, 2007.

[11] X. Sun and Y. Li, "Colloidal Carbon Spheres and Their Core/Shell Structures with Noble-Metal Nanoparticles," *Angew. Chemie Int. Ed.*, vol. 43, no. 5, pp. 597–601, 2004.

[12] A. Bhaumik, A. M. Shearin, R. Delong, A. Wanekaya, and K. Ghosh, "Probing the Interaction at the Nano–Bio Interface Using Raman Spectroscopy: ZnO Nanoparticles and Adenosine Triphosphate Biomolecules," *J. Phys. Chem. C*, vol. 118, no. 32, pp. 18631–

18639, 2014.

[13] H. T. Evans, “An X-ray diffraction study of tetragonal barium titanate,” *Acta Crystallogr.*, vol. 14, no. 10, pp. 1019–1026, 1961.

[14] N. M. Zali, C. S. Mahmood, S. M. Mohamad, C. T. Foo, and J. A. Murshidi, “X-ray diffraction study of crystalline barium titanate ceramics,” , pp. 160–163, 2014.

[15] G. K. Naik, S. M. Majhi, K.-U. Jeong, I.-H. Lee, and Y. T. Yu, “Nitrogen doping on the core-shell structured Au@TiO2 nanoparticles and its enhanced photocatalytic hydrogen evolution under visible light irradiation,” *J. Alloys Compd.*, vol. 771, pp. 505–512, 2019.

[16] J. G. Munguía-Lopez, E. Muñoz-Sandoval, J. Ortiz-Medina, F. J. Rodriguez-Macias, and A. De Leon-Rodriguez, “Effects of Nitrogen-Doped Multiwall Carbon Nanotubes on Murine Fibroblasts,” *J. Nanomater.*, vol. 2015, pp. 1–7, 2015.

[17] D. Geng *et al.*, “Nitrogen doping effects on the structure of graphene,” *Appl. Surf. Sci.*, vol. 257, no. 21, pp. 9193–9198, 2011.

[18] Z. Li *et al.*, “Highly luminescent nitrogen-doped carbon quantum dots as effective fluorescent probes for mercuric and iodide ions,” *J. Mater. Chem. C*, vol. 3, no. 9, pp. 1922–1928, 2015.

[19] J. Lu, Q. Zhang, J. Wang, F. Saito, and M. Uchida, “Synthesis of N-Doped ZnO by grinding and subsequent heating ZnO-urea mixture,” *Powder Technol.*, vol. 162, no. 1, pp. 33–37, 2006.

[20] J. Pokorný, U. M. Pasha, L. Ben, O. P. Thakur, D. C. Sinclair, and I. M. Reaney, “Use of Raman spectroscopy to determine the site occupancy of dopants in BaTiO 3,” *J. Appl. Phys.*, vol. 109, no. 11, p. 114110, 2011.

[21] Z. Ma, H. Ming, H. Huang, Y. Liu, and Z. Kang, “One-step ultrasonic synthesis of fluorescent N-doped carbon dots from glucose and their visible-light sensitive photocatalytic ability,” *New J. Chem.*, vol. 36, no. 4, p. 861, 2012.